Nguyen *et al. Energy Mater* 2023;3:300030
DOI: 10.20517/energymater.2023.11

Energy Materials

Review

Open Access

Check for updates

Challenges and design strategies for alloy-based anode materials toward high-performance future-generation potassium-ion batteries

An-Giang Nguyen[1], Rakesh Verma[2,*], Pravin N. Didwal[3], Chan-Jin Park[1,*]

[1]Department of Materials Science and Engineering, Chonnam National University, Gwangju 61186, Republic of Korea.
[2]Department of Chemistry, University of Allahabad, Prayagraj 211002, India.
[3]Department of Materials, University of Oxford, Oxford OX1 3PH, UK.

***Correspondence to:** Prof./Dr. Rakesh Verma, Department of Chemistry, University of Allahabad, Prayagraj 211002, India. E-mail: rakesh@allduniv.ac.in; Prof./Dr. Chan-Jin Park, Department of Materials Science and Engineering, Chonnam National University, Yongbong-ro, Buk-gu, Gwangju 61186, Republic of Korea. E-mail: parkcj@jnu.ac.kr

How to cite this article: Nguyen AG, Verma R, Didwal PN, Park CJ. Challenges and design strategies for alloy-based anode materials toward high-performance future-generation potassium-ion batteries. *Energy Mater* 2023;3:300030. https://dx.doi.org/10.20517/energymater.2023.11

Received: 27 Feb 2023 **First Decision:** 17 Mar 2023 **Revised:** 22 Apr 2023 **Accepted:** 5 May 2023 **Published:** 4 Jul 2023

Academic Editors: Yuping Wu, Federico Bella **Copy Editor:** Fangling Lan **Production Editor:** Fangling Lan

Abstract

Potassium-ion batteries (PIBs) are a promising candidate for low-cost and large-scale energy storage due to their abundant potassium resources. However, the potassiation-depotassiation of K^+ presents a significant challenge due to its large ionic radius, which results in the pulverization of active materials and poor cyclability. Thus, researchers are exploring anode materials with a high specific capacity, long cyclability, and excellent rate capability. In this context, alloy-type anode materials are exceptional candidates due to their high theoretical capacity and low working potential. Nonetheless, the large volume expansion of active materials limits their practical application. This review discusses various strategies for overcoming these challenges, including nanostructure design, heterostructure design, alloy engineering, and compositing. The review provides a comprehensive overview of the current state of research on alloy-based anodes for PIBs and offers insights into promising directions for future work toward commercializing PIBs.

Keywords: Alloy anode, high-performance anode, potassium-ion batteries

INTRODUCTION

Lithium-ion batteries (LIBs) have been widely used as a reliable energy resource for electronic devices and electric vehicles due to their high-energy density and long cycle life[1-5]. However, their feasibility for larger energy storage systems is limited by their inherent drawbacks, including high cost, safety issues, limited lithium resources, and concerns regarding human rights violations in the raw material mining process. As a result, researchers are exploring alternative candidates for LIBs, such as lithium-sulfur batteries[6,7], sodium-ion batteries (SIBs)[8], potassium-ion batteries (PIBs)[9], and safer LIBs that incorporate solid electrolytes[10-12]. Among these alternatives, SIBs and PIBs have attracted more attention as potential substitutes for LIBs due to their similarities in function[13]. As shown in Figure 1A, sodium and potassium are more abundant natural resources, with a respective crustal abundance of 2.36 wt% and 2.09 wt%[14]. In addition, the use of aluminum foil as the current collector for both SIBs and PIBs can help to further reduce the cost of the battery. Moreover, the standard reduction potential of K^+/K (-2.93 V *vs.* standard hydrogen electrode, SHE) is lower than that of Na^+/Na (-2.71 V *vs.* SHE), suggesting that PIBs may have a higher energy density than SIBs. Additionally, K^+ has weak Lewis acidity compared to Na^+, which reduces the solvation energy, thereby improving the ionic conductivity of the electrolytes[15,16]. As a result of these benefits, the development of PIBs has received significant attention.

Developing anode materials for PIBs is a significant challenge mainly due to the large ionic radius of K^+ (1.38 Å), which can damage the anode structure during cycling[15]. Various types of anode materials, such as intercalation, conversion, and alloy-type anodes, have been investigated. Among these, alloy-type anodes have garnered attention due to their low working potential and high theoretical capacity, which can enhance the energy density of practical PIBs. However, these anodes are prone to large volume expansion during potassiation and depotassiation, causing the anode to self-pulverize and lose contact with the current collector. To address these issues, several strategies have been developed, primarily focusing on nanostructure engineering, alloy composition (binary or ternary alloys), heterostructures (hybrids with other types of anodes), and composition with buffer materials. Properly structured anodes can mitigate volume expansion and promote the movement of electrons and ions, leading to improved rate capability and cyclability of the anode. Furthermore, optimizing binders and electrolytes can improve the electrochemical performance of alloy anode materials.

This review summarizes recent achievements in alloy-type anode materials for PIBs. To provide a comprehensive overview, the fundamental knowledge of PIBs and anode materials is summarized and evaluated, along with synthesis techniques and design methodologies. Additionally, possible strategies and perspectives are provided to expedite the research and development of alloy anodes. We aim to provide in-depth knowledge about the current state of alloy anodes, elucidating the development of robust, high-performance alloy anodes for PIBs and beyond.

FUNDAMENTALS OF ANODE MATERIALS

Working principle of potassium-ion batteries

Similar to LIBs and SIBs, PIBs operate based on the "rocking chair" working principle. To facilitate the development of PIBs, we first explore their fundamental components, as depicted in Figure 1B anode, cathode, and electrolyte. Generally, anode and cathode powders are mixed with a binder and conductive carbon before being coated onto the current collector. In PIBs, aluminum foil can be utilized as the current collector for both anode and cathode, reducing the overall weight of the battery and enhancing energy density. The electrolyte permeates a porous separator, which physically separates the anode and cathode to prevent internal short-circuiting while enabling K^+ ion transport. In the case of polymer and solid electrolytes, they can serve as both electrolytes and separators. During charging, K^+ ions diffuse from the

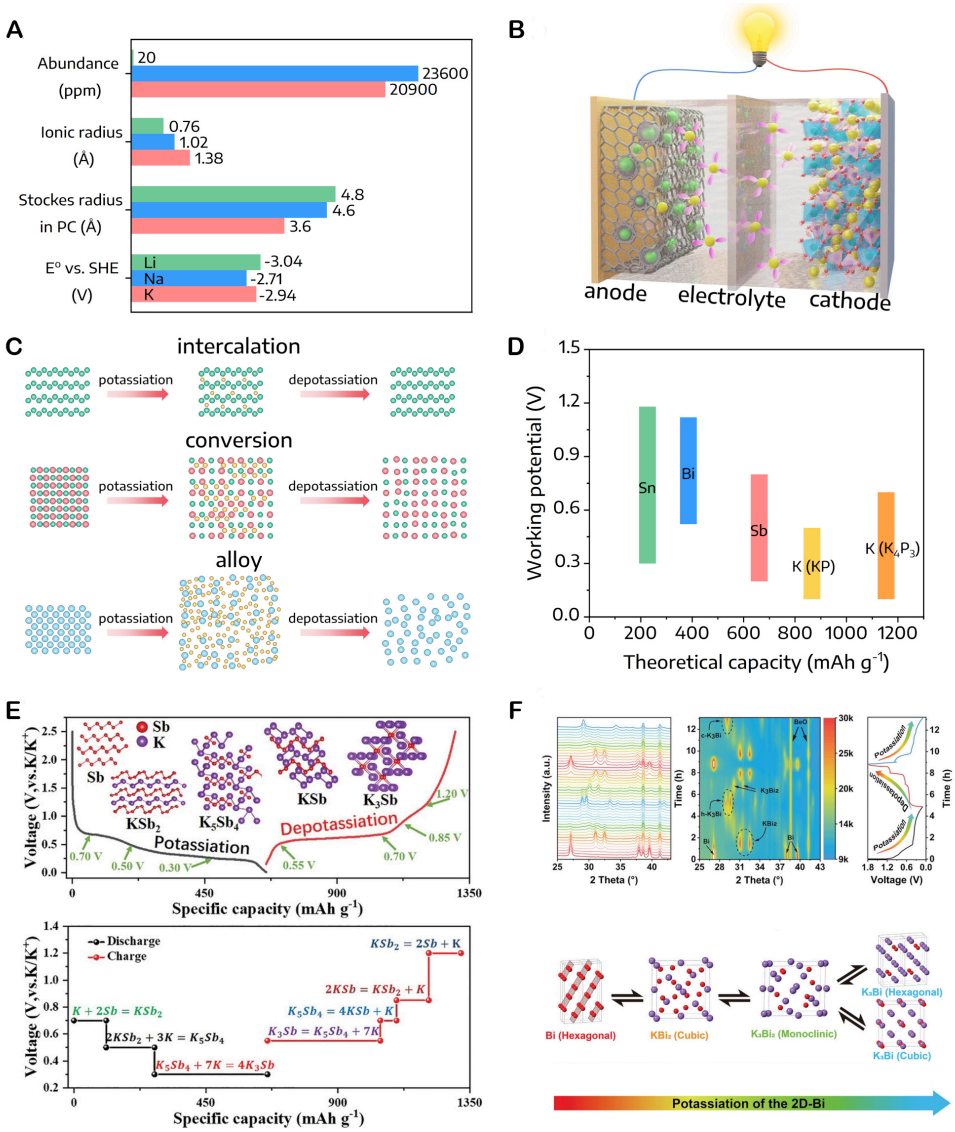

Figure 1. (A) Comparison of the basic properties of Li, Na, and K. (B) Schematic of the working principle of PIBs. (C) Illustration of the intercalation, conversion, and alloy types of PIB anodes. (D) Theoretical capacity and average voltage of various alloy anodes for PIBs. (E) Discharge-charge profiles and corresponding equilibrium potential (*vs.* K^+/K) obtained according to *ex-situ* XRD results and discharge-charge profiles of porous-Sb. Reprinted with permission from Ref.[23]. Copyright 2021, John Wiley and Sons. (F) Operando XRD analysis to investigate the structural evolution of the 2D-Bi anode for PIBs during the potassiation/depotassiation process. Reprinted with permission from Ref.[24]. Copyright 2022, John Wiley and Sons.

cathode to the anode through the electrolyte, and electrons are released, connecting to K^+ at the anode via the external circuit. This process converts external electrical energy into electrochemical energy. During discharging, the process is reversed: the K atom releases an electron and moves through the electrolyte from the anode to the cathode. At the cathode, K^+ recombines with the electron, supplying energy to the external load.

Requirement for anode

As mentioned above, anode materials for PIBs must meet the following requirements based on the working principle of PIBs: (i) exhibit good electronic or mixed ionic-electronic properties; (ii) have a high specific capacity, be lightweight, and have a low working potential with K^+/K to improve the working voltage and

energy density of full-cell PIBs; (iii) have a long cycle life; (iv) remain stable when in contact with electrolytes; and (v) utilize low-cost raw materials and synthesis routes.

Anode classification

Anode materials can be classified into three main categories based on the potasiation and depotasiation mechanism, as illustrated in Figure 1C: (i) intercalation; (ii) conversion; and (iii) alloy-type materials. Each type of material has its own unique set of advantages and disadvantages.

Intercalation anode materials, such as carbonaceous materials, possess interlayer gaps or voids suitable for K^+ intercalation-deintercalation during charge-discharge without undergoing significant structural changes, leading to stable cyclability[17,18]. However, their low specific capacity hinders their commercialization. In contrast, conversion-type anode materials, including transition metal oxides and sulfides, offer high specific capacity through multi-electron conversion reactions. Nonetheless, these materials exhibit a high potential plateau (> 1.0 V *vs.* K^+/K) and undergo considerable volume changes during cycling, presenting substantial challenges.

Alternatively, alloy-type anode materials rely on the alloying reaction between potassium and various elements in groups 14 and 15 or their derivatives to achieve a high specific capacity. Additionally, their relatively low potential plateau (< 1.0 V *vs.* K^+/K) facilitates the development of high-energy-density PIBs. Consequently, alloy-type anode materials have recently garnered significant research attention. However, similar to conversion-type materials, volume expansion during alloying/dealloying can cause active materials to pulverize, necessitating durable anode materials. Over the past few decades, numerous strategies have been developed that focus on (i) nanostructure design; (ii) composites with buffer materials; (iii) engineering alloys (binary or ternary alloys); and (iv) heterostructures (hybrids with other types of anodes). In this review, alloy-type anode materials are divided into two subgroups: (i) metal-metalloid, such as tin, antimony, bismuth, and their compounds (oxides, sulfides, and oxyhalides); and (ii) non-metals (phosphorus).

Reaction mechanism

Despite the challenges associated with the large ionic size of K^+, the solvated ion property of potassium can be beneficial for achieving reasonable storage capacity and cyclability with graphite and amorphous carbon anode materials. However, the low density of carbon anodes limits their practical applicability. Therefore, alloy-based anodes could be an attractive option due to their high theoretical specific capacity, high-energy density, and low operating potential, as depicted in Figure 1D.

In contrast to intercalation-based anodes, where the original crystal structure remains unaltered during potassiation/depotassiation, both alloying and conversion reactions result in phase transitions and structural changes that create new crystal phases through the reordering of atoms, as depicted in Figure 1C. Specifically, alloy anodes undergo a significant volume expansion during these processes. The reaction mechanism of M alloy anodes follows the reaction below:

$$\text{Potassiation: } xM + yK^+ + ye^- \rightarrow M_xK_y \quad (1)$$

$$\text{Depotassiation: } M_xK_y \rightarrow xM + yK^+ + ye^- \quad (2)$$

The reaction mechanism of alloy anodes involves multi-electron and K^+ reactions, making them highly attractive for their high theoretical capacities but also structurally destructive. Additionally, the phase

diagram can serve as a useful reference for predicting the intermediate stages occurring during alloying/dealloying processes. Among the alloy-based anodes for PIBs, Bi, P, Sn, and Sb are of particular interest due to their high theoretical capacity and energy density[19]. According to Kim *et al.*, Bi-, P-, Sn-, and Sb-based anodes form various alloy ratios with K and provide high theoretical capacity[20]. However, these alloys suffer from sluggish kinetics and significant volume growth, which remain a major challenge. To advance research on alloy-based anodes for PIBs, it is critical to examine current developments and offer potential solutions.

Sn is a promising anode material for PIBs with an acceptable capacity of 226 mAh g^{-1} (with the formation of KSn) and low operating potential (0.3 to 1.1 V *vs.* K^+/K)[21]. Sn alloying with K follows a two-step mechanism. It involves the initial potassiation of Sn to amorphous K_4Sn_9, followed by further potassiation to the KSn phase. The full potassiation results in a volume expansion of approximately 197%. Unlike the reaction of the Sn anode in LIBs and SIBs, the formation of the KSn phase as the end product limits the capacity of the Sn anode. Upon extracting K^+, the reverse reaction occurs at 0.75 and 1.1 V *vs.* K^+/K, leading to the full recovery of the Sn phase. This suggests a highly reversible alloying/dealloying reaction between Sn and K[22].

Conversely, Sb is a well-recognized anode material for high-energy-density PIBs. During potassiation, Sb forms three intermediate phases, namely KSb_2, K_5Sb_4, and K_3Sb, at distinct potentials ranging from 0.7 to 0.3 V, as depicted in Figure 1E[23]. During depotassiation, K_3Sb progressively releases K^+ ions to form K_5Sb_4, KSb, KSb_2, and Sb within the potential range of 0.55-1.2 V. Nevertheless, the slow diffusion rate of K in Sb crystalline structures results in increased polarization.

Bi is an appropriate alloy-based anode material for PIBs owing to its non-toxicity, large *c*-axis lattice spacing, and sufficiently high theoretical capacity. The potassiation/depotassiation mechanism of the Bi anode was investigated using operando XRD [Figure 1F][24]. During discharge, Bi initially alloys with K at a potential of 0.81 V, forming KBi_2. As the battery continues to discharge to 0.38 V and 0.23 V, a multiphase composition consisting of Bi, KBi_2, K_3Bi, and K_3Bi_2 coexists. Upon subsequent potassiation at 0.15 V, the multiphase fully converts to the hexagonal K_3Bi phase. In reverse, upon being charged to 0.57 V, K_3Bi fully transforms into K_3Bi_2. As the depotassiation process progresses, K_3Bi_2 further dealloys into KBi_2 and finally Bi at 0.76 and 1.16 V, respectively. Similar to Sb, Bi is also affected by the morphological change brought on by volume expansion (up to approximately 406%).

Phosphorus has a large theoretical capacity and low formation energies or potential of various K-P alloy phases, such as K_3P_{11}, K_3P_7, K_2P_3, KP, K_4P_3, and K_3P, which make phosphorus allotropes attractive for PIBs[21]. However, the use of P anodes in PIBs is becoming less popular due to a lack of accessible, inexpensive, and safe synthesis approaches. The reported Coulombic efficiency of the P anode is also unsatisfactory. Therefore, the development of safe and highly effective synthesis approaches for P anodes is essential. Moreover, Table 1 presents the physical and electrochemical properties of diverse alloying-type anode materials for PIB applications.

Challenges of alloy anode

Volume expansion

Figure 1C illustrates that the anode material M reacts with K^+ to form K_xM_y, as shown in reaction (1), resulting in significant volume and structural changes that lead to poor electrochemical performance. This reaction has three main consequences. Firstly, it pulverizes the anode materials and damages their original structure. Secondly, the contact between each active particle and between the anode and the current

Table 1. Physical and electrochemical properties of the alloying-type anode materials for PIBs

Material	Abundance (ppm)	Density (g cm^{-3})	Final alloying product	Theoretical capacity (mAh g^{-1})	Volume expansion (%)
Si	270,000	2.33	KSi	954	334
Ge	1.8	5.32	KGe	369	Unknown
Sn	2.2	7.31	KSn	226	~197
Sb	0.2000	6.69	K_3Sb	660	407
Bi	0.0480	9.78	K_3Bi	385	> 400
P	1,000	1.82	K_3P	≤ 2,596	593
			K_4P_3	1,154	293
			KP	865	190
Pb	1.4	11.34	KPb	126	> 259
Sb_2S_3	-	4.56	$K_3Sb + K_2S_3$	946	~300
Sb_2Se_3	-	5.81	$K_3Sb + K_2Se$	670	Unknown

collector is lost, which may reduce the electrical conductivity. Thirdly, the repeated volume change can also destroy the solid electrolyte interface (SEI) layer, leading to poor cyclability and increased consumption of active K^+ to be stabilized.

Unstable solid electrolyte interface layer

In PIBs, the SEI layer is crucial for battery performance. The SEI layer is formed when the lowest unoccupied molecular orbital of the electrolyte is lower than the Fermi level of the anode, and its function is to prevent side reactions between the anode and electrolyte[5]. However, in PIBs, the formation of the SEI layer is even more critical than in LIBs and SIBs due to higher chemical reactivity of potassium. Additionally, the SEI layer is more prone to redissolution in PIBs due to the higher solubility of SEI components in organic solvents. The formation of the SEI layer is more pronounced in full-cells than in half-cells since only a limited supply of potassium is available from the cathode side. A stable SEI layer is difficult to maintain in alloy anodes due to the large stress-strain generated during cycling, causing a breakdown of the SEI layer. This can lead to a range of underlying problems, such as anode pulverization, the formation of new SEI layers, and the thickening of the potassium diffusion barrier, all of which can cause degraded battery performance and continuous capacity decay.

Voltage hysteresis

Hysteresis, which refers to the loss of energy during the charging and discharging process, poses a significant challenge to the practical application of alloy anodes in PIBs. While there is limited research on the cause of voltage hysteresis in alloy anodes for PIBs, similarities between PIBs and LIBs or SIBs may provide some insights. The complexity of the alloying reaction process results in significant hysteresis and low energy efficiency. One of the most common characteristics of voltage hysteresis is the difference in the shape of the charge and discharge curves. The cause of voltage hysteresis is not well understood, but many studies have explained it from thermodynamic and kinetic perspectives. Potential causes of voltage hysteresis include sluggish ion diffusion and interface mobility, phase transformations, and mechanical strain caused by large-volume expansion. Furthermore, voltage hysteresis is closely linked to the formation of the SEI layer and surface stress, both of which are influenced by the chemomechanical behavior of the alloy anodes.

Unraveling electrochemical reaction mechanisms

The incomplete understanding of the charging mechanisms of most alloy anodes is hindering advancement in the field. A better understanding of the intermediate stages of the charging process is crucial to

comprehend the reasons behind the failure of the anodes. Unfortunately, current analytical techniques are not capable of providing a comprehensive understanding of the process, particularly in systems where both amorphous and crystalline phases are present. This knowledge gap presents significant challenges for the development and optimization of alloy anodes. Furthermore, it is common for the charging process in the first cycle to differ from subsequent cycles, indicating a different reaction pathway. Researchers are still investigating the origins and effects of this phenomenon on the performance of the anodes. The above investigations of alloy anodes highlight the need for a more profound comprehension of the reaction and failure mechanisms to avoid misinterpreting experimental results. Therefore, it is critical to develop new analytical techniques, such as *in-situ* and operando, to overcome current limitations and provide a complete understanding of the electrochemical mechanisms of alloy anodes.

SYNTHETIC METHOD OF ALLOY-BASED ANODE

In the literature, various methods have been investigated to synthesize alloy-based anode materials with different geometries and morphologies, which significantly affect their electrochemical performance. These methods can be classified into two approaches: top-down and bottom-up. The top-down approach involves using physical techniques to break bulk materials down into nanoparticles, but it may be less effective in achieving the desired particle size and shape. In contrast, the bottom-up approach starts from the atomic level and builds up to nanoparticles. By controlling the growth and assembly process of atoms and molecules, their morphology and size can be well-defined. In this section, we discuss several typical methods as follows:

High-energy ball milling

High-energy ball milling is a mechanochemical technique that can be used to synthesize nanopowders, alloys, and composites on a large scale. This method is effective in producing fine, homogeneous products with controlled microstructure and composition. During this process, powder precursors react with each other due to the high-energy collision caused by the motion of the balls, as depicted in Figure 2A. This energy can also generate chemical reactions. However, the morphology of the obtained product may be irregular, and the product may be contaminated by the balls. The milling process is influenced by several parameters, including the type, size, weight, and shape of balls, rotation speed, time, and atmosphere. One example of a material synthesized by high-energy ball milling is nanosized SnSe@C[25]. In this synthesis, SnSe powder and carbon black were pre-mixed and added to a sealed steel jar, along with stainless steel balls, in a powder/ball weight ratio of 1:20. The jar was sealed under an argon atmosphere to avoid any contaminants. As a result of the high-energy collisions, C-Sn and C-Se bonds were generated, which promote charge transfer and maintain the original structure of the SnSe@C nanocomposite during cycling [Figure 2A]. It is important to optimize the milling time since a short time may be insufficient to form a chemical reaction, while a long time may lead to product contamination and agglomeration. High-energy ball milling has also been used to synthesize other composites and alloys, such as Sb-C composite[26], Bi_2Te_3@C[27], and SnP_3/C composites[28]. Nonetheless, this approach necessitates an extended milling duration, and the substantial energy input may result in the introduction of defects and impurities within the alloy.

Hydrothermal/solvothermal methods

Hydrothermal/solvothermal methods are powerful techniques for synthesizing nanomaterials under high-pressure conditions, allowing control of the size, morphology, and crystallinity of the obtained materials by adjusting the type and ratio of precursors, temperature, pressure, filling percentage, time, surfactant, and solvent. This method has been successfully employed to develop alloy anode materials with suitable morphology, such as Sb single atoms and quantum dots@$Ti_3C_2T_x$[29], N, S, and F co-doping Sb@C[30], Sb/Sb_2S_3 nanorods embedded in the hollow carbon tube[31], Sb nanoparticles[32], and $CuCo_2S_4$

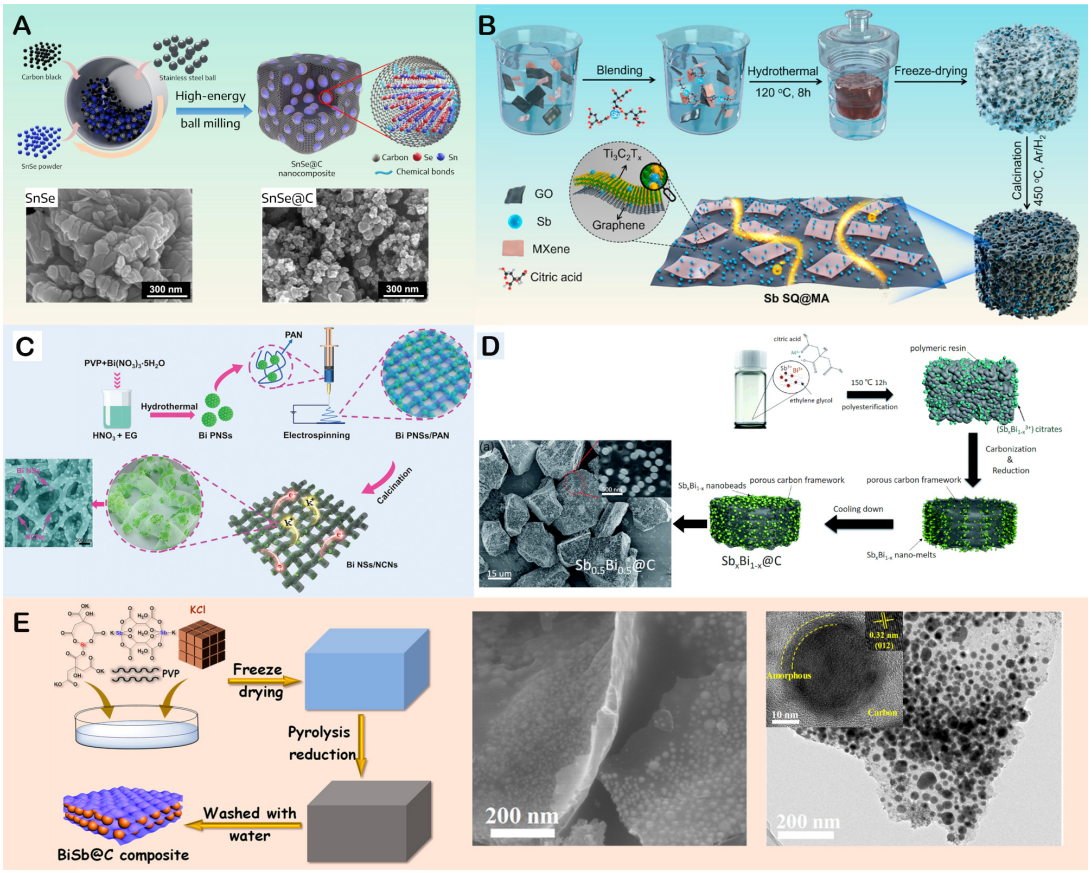

Figure 2. Illustration of the processes used to synthesize alloy anode for PIBs: (A) high-energy ball milling. Reprinted with permission from Ref.[25]. Copyright 2021, Elsevier. (B) hydrothermal. Reprinted with permission from Ref.[29]. Copyright 2022, American Chemical Society. (C) electrospinning. Reprinted with permission from Ref.[36]. Copyright 2021, John Wiley and Sons. (D) sol-gel. Reproduced from Ref.[41] with permission from the Royal Society of Chemistry. (E) freeze-drying. Reprinted with permission from Ref.[42]. Copyright 2020, American Chemical Society.

nanoparticles[33]. However, this approach may be time-consuming, necessitate a specialized reactor, and prove unsuitable for large-scale production.

Guo *et al.* co-decorated Sb single atoms and quantum dots on $Ti_3C_2T_x$ nanosheets using hydrothermal, freeze-drying, and calcination steps [Figure 2B][29]. The $Ti_3C_2T_x$ nanosheets contain abundant functional groups and Ti vacancies, which promote the adsorption of Sb^{3+}. Citric acid was used as a chelating agent to form Sb-citrate complexes and control Sb nucleation and growth. Under hydrothermal conditions, Sb-citrate complexes were weakened, and Sb^{3+} was gradually released. Then, both Sb^{3+} on the $Ti_3C_2T_x$ and in the solution was reduced to form Sb single atoms and quantum dots.

In contrast, Shi *et al.* used SiO_2@C as a template material to construct a porous structure without the freeze-drying step[30]. The SiO_2 template was etched by HF, leaving a carbon porous structure. In addition, allylurea precursors provided N and S heteroatoms doped on the carbon. While Sb^{3+} from the SbF_3 precursor was transferred to Sb_xO_y, the remaining F^- can also be dopped on the carbon materials. Sb_xO_y was further reduced to Sb by the heat treatment process.

Electrospinning

Electrospinning is a promising method for preparing novel nanofibers. In this technique, a polymeric mixture in a syringe is extruded by a pump through a metallic needle at a controlled rate to form a spherical droplet. At the same time, a sufficient voltage is applied to charge the droplet. When the electrostatic repulsion is stronger than the surface tension, the droplet deforms into an electrically charged conical shape called a Taylor cone. As a result, as-spun fibers erupt from the Taylor cone and are collected on the grounded collector[34]. Additionally, the properties of the as-spun fibers can be controlled by various parameters, such as solution properties (e.g., surface tension, viscosity, polymer type, dielectric constant of the solvent, and precursor ratio), working conditions (e.g., applied voltage, distance, and feeding rate), and environment (e.g., temperature and humidity). Due to these advantages, electrospinning is widely used to prepare 1D nanofibers with various structures, such as highly porous, core-shell, and hollow structures[35]. Additionally, it is important to note that this method may involve the use of hazardous solvents.

To be used as anode materials, pyrolysis of the precursors is typically needed after electrospinning. For example, Cui *et al.* reported the synthesis of ball-cactus-like Bi nanospheres embedded in N-rich carbon nanonetworks (Bi NSs/NCNs) via the electrospinning method, as shown in Figure 2C[36]. The Bi nanospheres were evenly distributed in the carbon nanonetworks in a size range of 2 to 140 nm, as observed in SEM and TEM images. This structure could reduce the diffusion pathways of K^+ ions and provide continuous electron transportation. However, the high Bi content of 59.2 wt% resulted in a brittle nanofiber and made it challenging to fabricate a free-standing electrode. In contrast, some investigations documented free-standing and flexible electrodes without the use of a binder, conductive carbon, or slurry-making steps when the active material content was too low (e.g., Sn or Sb wt% < 50 wt%)[37-40]. Unfortunately, the low content of active materials makes this strategy less appealing as it reduces the specific capacity of the materials. Additionally, the high carbon content may lower the initial Coulombic efficiency (ICE) of the composite due to the low ICE of carbon materials. Moreover, these materials have low tape density, which results in a reduced volumetric capacity.

Sol-gel method

The sol-gel method is a unique wet chemistry approach for material synthesis that is widely used due to its simplicity, low cost, high purity, and controllable composition and microstructure of materials. In general, it involves hydrolyzing the precursor, condensing it to form a sol, and then transferring it to a gel. Additionally, a chelating agent, such as citric acid, can be used to trap the metal when preparing a binary alloy to avoid the formation of multiple phases. On the other hand, the incorporation of chelating agents can also raise the cost and necessitate a carbonization process. Typically, He *et al.* reported Sb_xBi_{1-x} nanoparticles embedded in a 3D carbon matrix using the sol-gel method[41]. Thanks to this method, the obtained sample was composed of uniformly distributed Sb_xBi_{1-x} particles with a size of 200 nm in the carbon matrix, as shown in Figure 2D. Additionally, in several studies, both hard-template and soft-template approaches have been incorporated and assisted by freeze-drying to construct highly porous materials, which will be introduced and discussed in the following section.

Freeze-drying

Freeze-drying is a powerful technique for producing porous materials at low temperatures that prevent the structure from collapsing during solvent removal. Generally, the precursor solution is cooled below the triple point of the solvent to ensure sublimation occurs rather than melting, and a vacuum is applied to accelerate the sublimation step. Nonetheless, the process necessitates specialized equipment and can span several hours or even days, contingent upon the material being synthesized. In particular, Xiong *et al.* used this method to synthesize Bi-Sb alloy nanoparticles encapsulated in a porous carbon nanosheet [Figure 2E][42]. As revealed by SEM and TEM analysis, BiSb alloy nanoparticles were evenly distributed in

the hierarchical nanosheet carbon, which is believed to enhance the electrochemical performance of anode materials.

Carbonization

At the end of most of the methods discussed above, carbonization is a crucial step required to reduce metal ions, carbonize organic precursors, and improve crystallinity. Depending on the nature of the materials, the temperature, time, and atmosphere of this process can be adjusted accordingly. For example, in the case of the sample shown in Figure 2E, after the freeze-drying step, the material was carbonized at a temperature of 600 °C for 5 h under a mixture of Ar/H_2. As a result, Bi^{3+} and Sb^{3+} were reduced to form BiSb alloy, and the organic part was pyrolyzed to carbon. Higher treatment temperatures may induce more graphitic carbon, which improves electron conductivity. However, it may also cause the agglomeration of nanoparticles and the collapse of the carbon matrix. Therefore, careful investigation and adjustment of the parameters are necessary.

Overall, each method listed in Table 2 presents its own advantages and disadvantages. The choice of a synthesis technique depends on the specific requirements of the application, such as the desired microstructure, cost, and production scale.

RECENT PROGRESS IN ALLOY-BASED ANODE MATERIALS

As mentioned in the Anode classification section, various strategies have been developed to overcome the challenge of significant volume variation in alloy anodes, including the use of nanostructured materials, engineering alloys (binary or ternary), heterostructures (hybrids with other types of anodes), and compositions with buffer materials. These strategies are discussed in detail below.

Metal-metalloid and their compounds

Nanostructure design of pure metal anode-metalloid type

The electrochemical properties of anode materials are significantly influenced by their diverse nanostructures, encompassing 0D, 1D, 2D, and 3D configurations. Specifically, 0D nanoparticles exhibit short migration pathways in all directions, while their nanoscale size offers additional void volume to accommodate substantial volume changes. In contrast, 1D and 2D structures enable rapid electron transport along their respective dimensions and short ion migration pathways along the remaining axis. Regarding 3D structures, their properties are dependent on the specific morphology. Generally, 3D structures not only facilitate continuous electron transport networks but also minimize the volume changes of active materials.

To demonstrate the benefits of nanostructuring, Imtiaz *et al.* used a vacuum-based thermal evaporator to decorate Sb on the surface of $Cu_{15}Si_4$ nanowires on a Cu mesh substrate ($Sb@Cu_{15}Si_4$)[43]. This structure not only provided a buffer zone for the Sb active material but also increased the contact area, reducing the diffusion length of K^+ [Figure 3A]. As a self-supported anode material, the $Sb@Cu_{15}Si_4$ array maintained a specific capacity of 250.2 mAh g^{-1} at 200 mA g^{-1} after 1,250 cycles, corresponding to a capacity retention of 65%. However, the complexity of the method and the large percentage of $Cu_{15}Si_4$/Cu mesh used as the current collector may limit its further application.

The surface-area-to-volume (SV/A) ratio is an essential parameter that depends on the morphology of anode materials and plays a crucial role in determining their electrochemical properties. A larger SV/A ratio may offer more pathways for electrolyte penetration, reducing the diffusion length. However, it can also consume more electrolytes and limit the migration of K^+ ions of the cathode to construct the SEI layer. This

Table 2. Comparison of the properties of various synthesis techniques, providing an overview of their respective advantages and disadvantages

Synthesis methods	Advantages	Disadvantages	Ref.
High-energy ball milling	- Cost-effective and straightforward approach. - Applicable for both dry and wet conditions. - Capable of producing nanoparticles with a size range of 2-20 nm, where the rotation speed of the balls influences particle size. - Features closed-loop grinding, operating under controlled conditions, and minimal dust generation	- Exhibits low efficiency and relatively high-energy consumption. - The procedure is time-intensive. - The resulting nanomaterial shape is irregular due to the less advanced nature of the process. - Prone to high levels of contamination	[25-28]
Hydrothermal/Solvothermal methods	- Straightforward, cost-effective, and user-friendly synthesis approach. - Morphology is controlled by synthesis parameters. - Capable of producing high-quality one-dimensional (1D) nanostructures, especially nanorods. - Facilitates control over particle size and shape. - Simple incorporation of dopants through the addition of chemicals	- Requires high temperature, high pressure, and an extended reaction time. - Necessitates the use of an expensive autoclave. - Challenges in attaining uniform particle size. - Presents safety concerns. - For the solvothermal process, increased pressure and reaction temperatures are needed, along with the use of organic solvents	[29-32]
Electrospinning	- Straightforward fabrication of composites. - High efficiency. - Suitable for mass production. - Simplified process.	- Limited control over the porosity of the structure. - Utilization of harmful solvents	[34-36]
Sol-gel method	- Homogeneous mixing at the atomic or molecular level. - Reduced heating time. - Enhanced crystallinity. - Nanometer-level particle size. - Even particle distribution. - Exceptional productivity efficiency. - Elevated chemical reactivity of precursors owing to the solution-phase process	- Costly raw materials. - Extended process durations	[41]
Freeze-drying	- Easy handling. - Long-term storage	- Elevated operating expenses. - Intricate procedure	[42]

principle was demonstrated by Cheng *et al.*, who synthesized and characterized 0D nanoparticles, 1D nanobranches, 2D nanosheets, and 3D porous Bi anode [Figure 3B][24]. After cycling, the 0D, 1D, and 3D Bi structures lost their contact, whereas the 2D-Bi maintained their original shape, indicating its stable structure against large volume expansion. Consequently, 2D-Bi exhibited the most stable cyclability at 10 A g^{-1} with the highest capacity retention of 94%. Similarly, Yang *et al.* investigated 0D, 2D, and 3D Sb materials and found that 2D Sb exhibited the best electrochemical performance, demonstrating the advantage of the 2D structure[44]. Moreover, Xu *et al.* coated 2D Bi with 4.9 wt% of N-doped carbon (2D Bi@NOC) derived from polydopamine (PDA)[45]. The synergistic effect of the 2D Bi and ultrathin N-doped carbon coating layer allowed 2D Bi@NOC to deliver excellent cyclability and rate capability compared to both bulk 2D Bi and Bi. Specifically, as shown in Figure 3C, 2D Bi@NOC maintained a high specific capacity of 341.7 mAh g^{-1} after 1,000 cycles at 10 A g^{-1} and provided a specific capacity of 220.6 mAh g^{-1} at an ultrahigh specific current of 50 A g^{-1}.

Additionally, 3D structures may possess an interconnected porous architecture, which can offer internal volume to reduce the effect of volume expansion and facilitate electrolyte penetration to promote high electron and ion diffusion. Liu *et al.* reported a hydrothermal method to synthesize honeycomb-like interconnected porous Sb[23]. Under high pressure and temperature, micro-sized Sb could react with H_2O and saturated O_2 to generate water-soluted H_2SbO_6 as a product, and then unreacted and porous Sb was constructed. The porous structure could be adjusted via reaction time, as shown in Figure 3D, and the optimized time was reached at 96 h. Beyond 96 h, the porous structure collapsed due to the high energy of

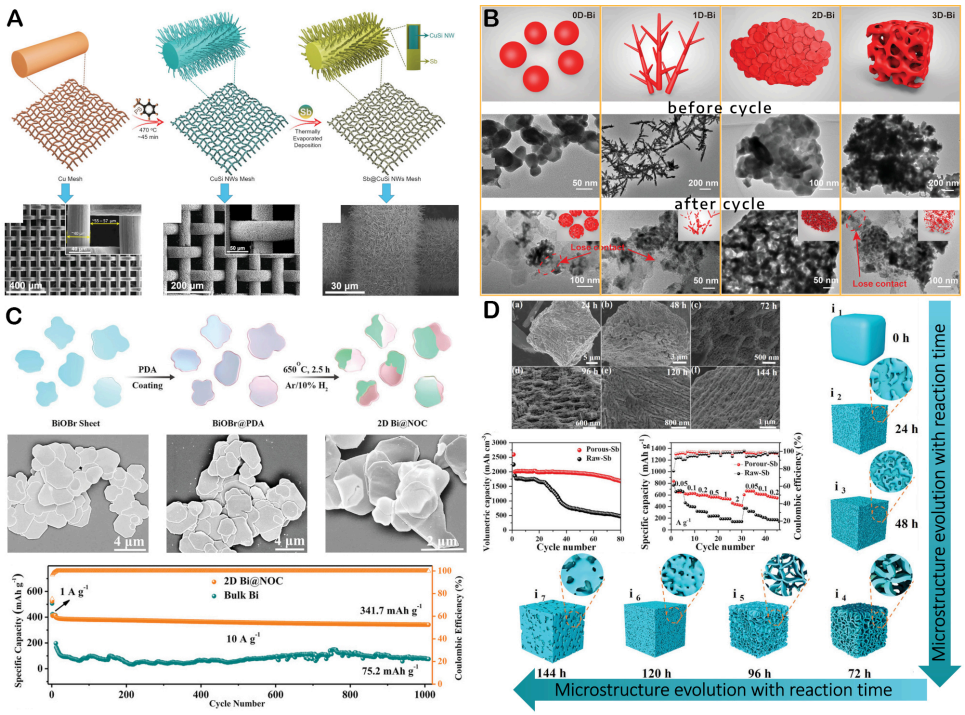

Figure 3. Schematic illustration of (A) the synthesis of the $Cu_{15}Si_4$ NW array current collector and thermally evaporated deposition of Sb with associated SEM pictures. Reprinted with permission from Ref.[43]. Copyright 2022, John Wiley and Sons. (B) An Illustration and TEM pictures of the 0D-Bi, 1D-Bi, 2D-Bi, and 3D-Bi taken before and after cycling. Reprinted with permission from Ref.[24]. Copyright 2021, John Wiley and Sons. (C) Illustration of the fabrication of the 2D Bi@NOC with corresponding SEM images and cyclability of 2D Bi@NOC. Reprinted with permission from Ref.[45]. Copyright 2022, John Wiley and Sons. (D) SEM images and microstructural evolution of micro-sized Sb samples at various reaction times. Reprinted with permission from Ref.[23]. Copyright 2022, John Wiley and Sons.

atoms on the grain boundaries, making them prone to etching and expansion to internal atoms over time. The optimized porous Sb anode exhibited a superior specific capacity of 550.6 mAh g^{-1} after 80 cycles at 50 mA g^{-1} and rate capability than those of raw Sb. However, the cyclability of porous Sb was still unsatisfactory, even when using a high-concentration electrolyte of 4 M KFSI in dimethyl ether (DME) and elastic polyacrylic acid (PAA). Therefore, further investigation of the porous structure of Sb is needed. Another approach to synthesizing 3D nanoporous Sb is the dealloying of Zn-Sb alloy under high temperature and vacuum conditions, as reported by An *et al.*[46].

Composite anode

Achieving extraordinary electrochemical performance using pure metals or metalloids as anode materials is quite challenging. Therefore, the introduction of another active or inactive buffer material could provide mechanical support to accommodate the volume change of alloy-type anodes. However, the selection of buffer materials should consider their relationship with the energy density of the final composite. Carbonaceous buffer materials are widely used due to their lightweight, which not only improves the electrical conductivity but also provides space against the volume expansion of the main active materials.

For example, Verma *et al.* synthesized Sb nanoparticles encapsulated in nitrogen-doped porous carbon (Sb@NPC) as an anode material for PIBs [Figure 4A][47]. By controlling the Sb_2O_3 and PVP precursor ratio, the amount of carbon was investigated. Sb@NPC-2 with 60.355 wt% of Sb exhibited the best electrochemical properties, delivering a high specific capacity of 360.8 mAh g^{-1} after 500 cycles at 800 mA g^{-1}. However, the cyclability and rate capability of Sb@NPC-1 with 78.766 wt% of Sb gradually degraded, indicating an

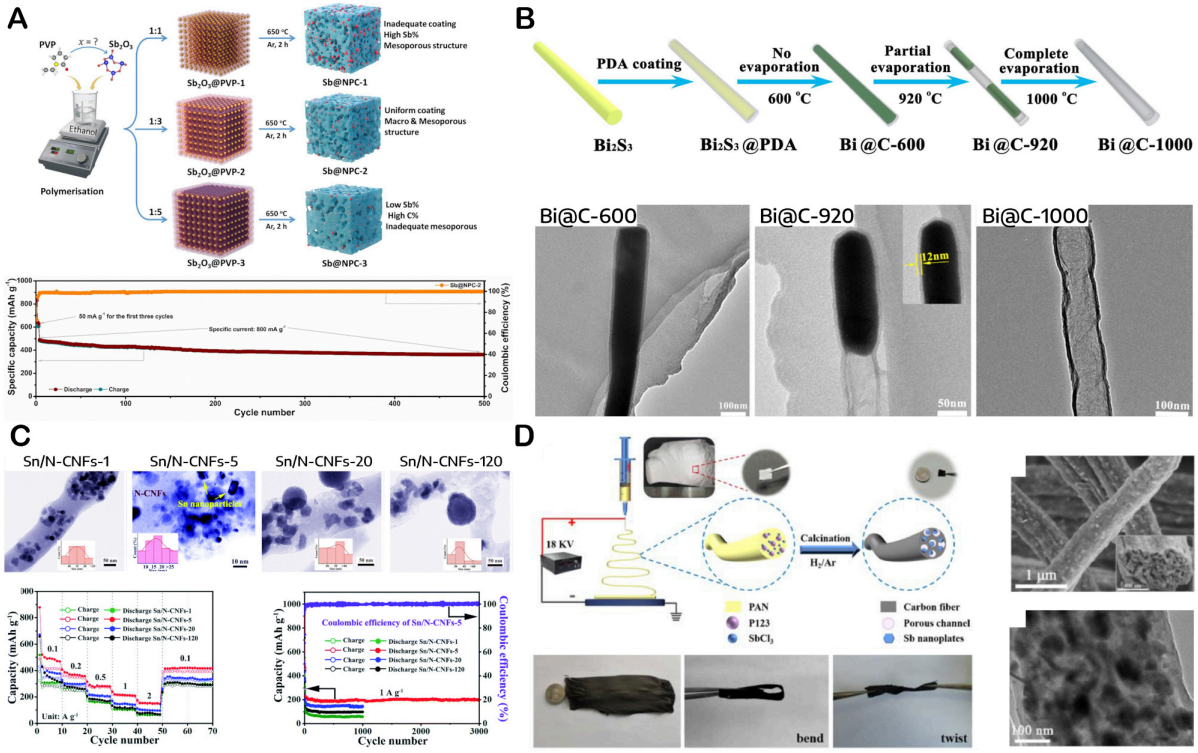

Figure 4. Schematic for the synthesis route of (A) Sb@NPC and its cyclability. Reprinted with permission from Ref.[47]. Copyright 2022, Elsevier. (B) Bi@C-600, Bi@C-920, and Bi@C-1000 with corresponding SEM images. Reprinted with permission from Ref.[55]. Copyright 2020, Elsevier. (C) TEM images with the particle size distribution of Sn/N-CNFs-1/5/20/120 and their electrochemical performance. Reproduced from Ref.[38] with permission from the Royal Society of Chemistry. (D) Schematic diagram of the preparation process of Sb@PCNFs with SEM and TEM images and digital photos of Sb@PCNFs at different states. Reprinted with permission from Ref.[40]. Copyright 2022, Elsevier.

insufficient amount of carbon buffer layer that could not resist the huge volume change of Sb. In contrast, the highest amount of carbon in Sb@NPC-3 lowered the specific capacity of the anode, as the capacity contribution of carbon was much lower than that of Sb. Therefore, Sb@NPC-2 exhibited outstanding performance due to the synergistic effect of the well-interconnected 3D Sb@NPC in which Sb nanoparticles were well-distributed in the NPC buffer material and the proper amount of NPC in Sb@NPC-2. Similar approaches were also reported, such as carbon sphere-confined Sb[48], spindle-like structured Bi@N-doped carbon[49], Bi@N-doped carbon[50], bismuth nanoparticles embedded in N-doped porous carbon[51], and bismuth nanoparticles confined in carbon nanospheres[52]. Moreover, MOF[32] and MXenes[29,53,54] can also be used as buffer materials.

As previously mentioned, the 1D structure is advantageous for both ionic and electron conduction; therefore, extensive research efforts have been devoted to investigating this unique structure. Xiang *et al.* synthesized hollow Bi@C nanorods[55]. As shown in Figure 4B, PDA-wrapped Bi_2S_3 nanorods were annealed at various temperatures. At 600 °C, Bi_2S_3@PDA was converted to a Bi@C-600 core-shell structure. Bi in the core could partially eliminate at a higher temperature of 920 °C to construct the Bi@C-920 York-shell structure. However, when the temperature was further increased to 1,000 °C, almost all of the Bi evaporated, greatly decreasing the specific capacity of the anode. In addition to the advantages of the 1D core-shell structure, the York-shell provides sufficient voids inside the shell to mitigate the pulverization of active particles during the alloying-dealloying process, thereby improving the stability of the anode during cycling. Consequently, Bi@C-920 exhibited superior cycling performance compared to the others. Moreover, the

void space can be further optimized via treatment temperature and time to maximize the specific capacity of the materials. Similarly, Sb/Sb_2S_3 nanorods embedded in a hollow carbon tube[31] and hollow carbon-confined Bi nanorods[56,57] were also reported.

Another approach to preparing 1D structures is using the electrospinning method. For example, Li *et al.* used this method to synthesize porous Sn nanospheres/N-doped carbon nanofibers (Sn/N-CNFs), as shown in Figure 4C[38]. However, their strategy is similar to the one used to synthesize Bi NSs/NCNs shown in Figure 2C, and the resulting Sn/N-CNFs may break down into nanorods during the slurry-making step, making the entitled nanofibers ambiguous. Notably, porous SnO_2 was used as the Sn precursor, which could break down to approximately 15 nm Sn particles after carbonization. The carbonization time varied from 1 to 120 min to obtain Sn/N-CNFs-1, Sn/N-CNFs-5, Sn/N-CNFs-20, and Sn/N-CNFs-120, respectively. Longer carbonization times induced more graphitic carbon, which improved the electronic conductivity, as confirmed by Raman analysis. However, longer carbonization times also provided sufficient energy to agglomerate and diffuse Sn to the surface of the carbon fibers [Figure 4C]. Consequently, Sn/N-CNFs-5, with 44.2 wt% of Sn, was the optimized sample that delivered a stable specific capacity of 198.0 mAh g^{-1} at 1 A g^{-1} after 3,000 cycles. Unfortunately, its specific capacity is still too low to meet the requirements for high-energy-density PIBs.

Furthermore, electrospinning can also be used to fabricate flexible anode materials. For instance, Chen *et al.* prepared flexible, free-standing, and binder-free Sb nanoplates encapsulated in porous carbon nanofibers (Sb@PCNFs), as presented in Figure 4D[40]. However, as mentioned earlier, Sb@PCNFs contained only 21.6 wt% of Sb, which means that carbon may act as the main component. Specifically, antimony chloride ($SbCl_3$) and polyacrylonitrile (PAN) were dissolved in N,N-dimethylformamide (DMF), with pluronic (P123) added as a porous agent. The Sb nanoparticles were evenly distributed in the multichannel nanofibers, which provided the extra void needed to buffer the large volume expansion of Sb. This structure also provided pathways for electrolyte penetration, which shortened the diffusion lengths of K^+. Moreover, Sb@PCNFs still maintained their flexibility even after bending or twisting, highlighting the advantages of this strategy [Figure 4D] Similarly, Ouyang *et al.* reported bismuth nanoparticles encapsulated in mesoporous carbon nanofibers, with an optimized 44.2 wt% Bi, as binder-free anode materials[58].

Engineering alloys

In recent years, engineering binary or ternary alloys has emerged as an effective approach to mitigate the severe volume expansion and enhance the electrochemical reaction kinetics of anode materials. These alloys can be formed by combining metal and metalloid elements with either electrochemically active or inactive elements. For example, SnSe[25], SnSb[59,60], SnTe[61], SbBi[62-65], Sb_2Se_3[66], Bi_2Se_3[67], $BiSbSe_3$[68], Co-Sb[69], $FeSb_2$[70], and NiSb[71] are some examples of such alloys. These alloys can be further combined with other strategies, such as carbon coating, nanostructure design, and electrolyte optimization, to improve the cyclability of anode materials. A range of methods has been employed to synthesize these alloys, including sol-gel, ball milling, spray method, precipitation, selenization, electrospinning, hydrothermal, and carbonization.

For active materials, binary or ternary compounds can achieve high theoretical specific capacity through a multi-electron transfer mechanism. Additionally, each element can buffer the other by alloying/dealloying with K^+ at different potentials, thereby substantially reducing the effect of volume expansion. The synergistic effect of these systems may result in excellent cyclability and rate capability. For instance, BiSb nanoparticles encapsulated in tremella-like carbon microspheres (BiSb@TCS) were synthesized by the KCl template-assisted spray method[63]. During the spraying process, the precursor solution transformed into KCl@BiSb@TCS microspheres [Figure 5A] After removing the KCl template through a washing step,

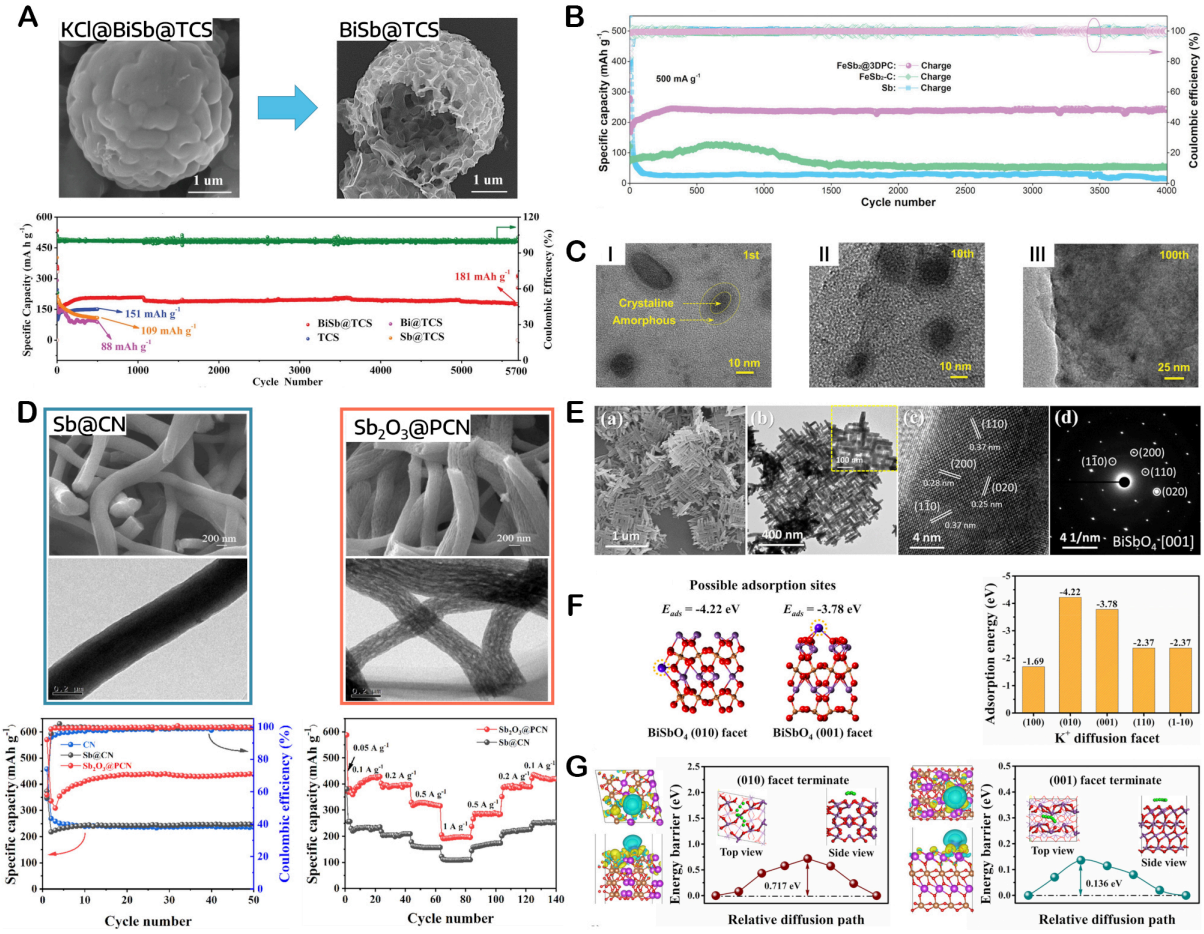

Figure 5. (A) SEM image of the carbonized microsphere showing the cyclability of BiSb@TCS before and after template-removing using (KCl@BiSb@TCS). Reprinted with permission from Ref.[63]. Copyright 2021, John Wiley and Sons. (B) Long cycle performance of the $FeSb_2$@3DPC, $FeSb_2$-C, and Sb anodes at 500 mA g^{-1}. (C) EM images of the potassiated FeSb2@3DPC sample in the (I) 1st, (II) 10th, and (III) 100th cycles. Reprinted with permission from Ref.[70]. Copyright 2022, John Wiley and Sons. (D) Comparison of the cyclability and rate capability of Sb@CN and Sb_2O_3@PCN using SEM and TEM images. Reprinted with permission from Ref.[72]. Copyright 2023, Elsevier. (E) The morphology of the $BiSbO_4$ network, as shown in SEM and TEM images. (F) Adsorption energies according to various exposed facets of the $BiSbO_4$ network. (G) Analysis of the differential charge density showing the energy barrier and diffusion path in the top and side views of the (010) and (001) facets. Reprinted with permission from Ref.[73]. Copyright 2022, American Chemical Society.

BiSb@TCS porous hollow microspheres were obtained, which were designed to suppress the disadvantages of BiSb anode. As a result, the BiSb@TCS electrode exhibited a stable capacity of 181 mAh g^{-1} at 2 A g^{-1} after 5,700 cycles, with a capacity retention of approximately 100%. In contrast, the Bi@TCS and Sb@TCS exhibited poorer cyclability, which highlights the advantages of the BiSb binary compound.

Incorporating inactive elements can improve the electronic conductivity, provide buffer areas, and significantly mitigate the volume expansion, ultimately leading to improved cyclability of the anode. However, inactive metals can significantly reduce specific capacity compared to carbon materials. For instance, $FeSb_2$ nanoparticles encapsulated in a 3D porous carbon framework ($FeSb_2$@3DPC) were synthesized using NaCl template-assisted freeze-drying, followed by a carbonization process[70]. The resulting structure had uniformly distributed $FeSb_2$ nanoparticles with an average size of 36.4 nm in a 3D porous carbon matrix. Due to its unique structure, $FeSb_2$@3DPC displayed a specific capacity of

242 mAh g^{-1} at 500 mA g^{-1} after 4,000 cycles with no significant degradation [Figure 5B] However, a stable capacity was only achieved after approximately 300 initial cycles. This phenomenon was attributed to the higher density of the orthorhombic $FeSb_2$ (8.09 g cm^{-3}) compared to that of hexagonal Sb (6.697 g cm^{-3}), which may slow down the diffusion of K^+. This was further explored by TEM analysis of the $FeSb_2$@3DPC structure at various cycles [Figure 5C] In fact, $FeSb_2$ had a core-shell structure with a potassiated outer shell covering the unreacted $FeSb_2$ core after the first potassiation step [Figure 5C(I)] The core-shell structure gradually dispersed and self-pulverized to reduce particle size during cycling [Figure 5C(II)] Consequently, $FeSb_3$ could completely react with K^+ and deliver a stable specific capacity [Figure 5C(III)] The electrochemical impedance spectra also revealed that the cell resistance became stable after 250 cycles, which is consistent with other analyses.

Oxide compounds

Oxide materials exhibit (de-)potassiation based on both conversion and alloying mechanisms, which involve a higher number of electrons participating in the reaction, leading to their high theoretical specific capacity. However, besides the disadvantages of alloy metals, oxide anodes may form irreversible products, such as K_2O, which consume the limited K^+ resource, especially in full-cell configuration. Moreover, the insulating property of metal oxides also limits their electrochemical performance. Therefore, innovative structural design and coating layers may be necessary to overcome these challenges. For instance, Sb-based as-spun fibers were calcined in the air instead of an inert atmosphere to produce Sb_2O_3 embedded in porous carbon nanofibers (Sb_2O_3@PCN) [Figure 5D][72]. Both Sb@CN and Sb_2O_3@PCN were synthesized by calcination in N_2 and air atmosphere, respectively. As observed in Figure 5D, the SEM and TEM images of Sb_2O_3@PCN revealed a porous structure, while Sb@CN was smooth. The porous structure of Sb_2O_3@PCN shortened the diffusion pathways of K^+ and delivered a higher specific capacity for both cyclability and rate capability. Furthermore, the gap between each step in the rate capability suggested that Sb_2O_3@PCN may have more polarization than Sb@CN. In another study, Chang *et al.* synthesized a $BiSbO_4$ nanonetwork via hydrothermal methods[73]. The $BiSbO_4$ nanonetwork was composed of interwoven $BiSbO_4$ nanorods, forming a meshwork [Figure 5E]. This structure reinforced the mechanical properties and provided conduction pathways for the anode materials. According to TEM analysis in Figure 5E, the $BiSbO_4$ nanorods preferred to grow along the [200] direction, exposing the (001) facet. Additionally, a DFT calculation was performed to investigate the favorable facet. Regarding the adsorption energy, the (010) facet exhibited the lowest adsorption energy of -4.22 eV, slightly lower than that of the (001) facet. This finding suggested that the (010) facet may easily adsorb K^+ to its surface [Figure 5F]. However, the energy barrier for K^+ diffusion in the (010) and (001) facets was 0.717 and 0.136 eV, respectively, as shown in Figure 5G. Therefore, the (001) facet may promote K^+ adsorption and diffusion, improving the kinetic of redox reaction when both adsorption energy and energy barrier are considered. The synergistic effect of architecture and crystal facet resulted in a specific capacity of 256.5 mAh g^{-1} at 500 mA g^{-1} after 1,000 cycles for the $BiSbO_4$ nanonetwork.

Sulfide compounds

Sulfide compounds have shown promising potential as anode materials for PIBs due to their high theoretical capacity. However, they suffer from several limitations, including volume expansion, low electrical conductivity, and polysulfide dissolution, which degrade their performance. To overcome these challenges, many approaches have been investigated, primarily focusing on structural design and composite materials. Recent studies have reported on several composites, including Sb_2S_3@Mxene composite[53], SnS@carbon nanofiber[74], SnS@multichannel carbon nanofibers[75], Bi_2S_3@graphene[76], yolk-shell Sb_2S_3@N, S-doped carbon nanorod[77], york-shell SnS_2@N, and S co-doped carbon fibers[78].

For example, SnS_2@N, S co-doped carbon core-shell flexible nanofibers (SnS_2@NSC CSN) were reported, which offer several advantages, such as providing a continuously conductive network and eliminating the effects of volume change and polysulfide dissolution through a core-shell structure [Figure 6A][78]. The SnS_2@NSC CSN with a thickness of 30 μm exhibits a unique hierarchical architecture of SnS_2@NSC york-shell structure along 1D carbon nanofibers, as shown in SEM images [Figure 6A]. Additionally, SnS_2 york was highly porous, as observed by TEM, providing double protection by both ultrafine nanocrystals of SnS_2 and the york-shell structure to adapt to the huge volume change of SnS_2. To highlight the unique structure of SnS_2@NSC CSN, we also synthesized SnS_2/NSC nanofibers without a york-shell structure (SnS_2/NSC SF) and SnS_2/C powder. The SnS_2@NSC CSN anode exhibited outstanding performance in terms of rate capability and cyclability, maintaining a specific capacity of 205.3 mAh g^{-1} at 2.0 A g^{-1} after 2,000 cycles, with a capacity retention of 75.4%, benefiting from its well-designed architecture. However, similar to other flexible carbon nanofibers, it also has a high carbon content of approximately 68 wt% and low tap density.

Oxyhalide compounds

Oxyhalide compounds are promising candidates for high-capacity anode materials. However, they face challenges similar to those encountered by alloy-type anodes. To address these issues, we explored the use of nanocrystal bismuth oxyhalide/RGO (S-BiOCl-RGO) as a free-standing anode with a high loading mass of approximately 4.21 mg cm^{-2}[79]. The percent of BiOCl in S-BiOCl-RGO was 67 wt%, making this approach more attractive and scalable than the electrospinning approach for utilizing active material content and tap density. Ultrasmall (approximately 6 nm) BiOCl particles were uniformly anchored in RGO. For comparison, BiOCl/RGO with a larger size of approximately 80 nm and bare BiOCl were also cycled. Notably, as shown in Figure 6B, S-BiOCl-RGO delivered specific capacities of 521, 480, 445, 409, 351, 297, and 205 mAh g^{-1} at 0.05, 0.1, 0.2, 0.5, 1, 3, and 5 A g^{-1}, respectively. Moreover, it remained stable for up to 3,000 cycles at 5 A g^{-1} with a high-capacity retention of 94.7%. The rate capability and cyclability of S-BiOCl-RGO were much better than other materials, including Bi-metal. Furthermore, S-BiOCl-RGO possessed a high volumetric capacity of 1,148 mAh cm^{-3}, benefitting from its free-standing, high packing density of 2.31 g cm^{-3} and mass loading of 4.21 mg cm^{-2}. This approach may provide insights for improving the specific capacity of alloy-based anode materials. The reaction mechanism and morphology evolution of S-BiOCl-RGO were studied using both operando XRD and *ex-situ* TEM. In particular, BiOCl was converted to Bi, K_2O, and KCl, forming a Bi alloy with potassium (K_3Bi) at the end of the discharge stage [Figure 6C]. Conversely, K_3Bi gradually dealloyed to release 3 K^+ and form K_2Bi and Bi. At the end of the charge stage, Bi reacted with K_2O and KCl to obtain BiOCl and 3 K^+ [Figure 6C]. A total of 6 K^+ and 6 electrons were involved in the redox reaction, explaining the high capacity of BiOCl. Similarly, a $Sb_4O_5Cl_2$-MXene composite as an anode material was reported[54].

Heterostructure

Recently, heterostructures have received significant attention as a means to improve the electrochemical performance of anode materials by increasing the rate of the redox reaction. Specifically, the Fermi energy level is shifted when electron transfer occurs between the heterostructures, generating additional electronic states. This results in a reduction in the energy barrier and acceleration of the kinetics for K^+ diffusion. Metal oxides, sulfides, and selenides are the main materials used for heterostructures, such as Bi_2S_3/Bi_2Se_3[80], Sb/MoS_2/C[81], *etc*. Currently, the heterostructure of metals or their oxide offers some attractive properties. Combining a metal with its oxide or another metal (e.g., Se) can be easily achieved through oxidation or selenization. For example, a Se@Sb@C heterostructure and a Sb_2Se_3@C composite were synthesized using a selenization process in open- and close-crucibles, respectively[82]. In a close-crucible, Se reacted with Sb to form Sb_2Se_3 under high vapor pressure of Se evaporation. During this process, Sb_2Se_3 grew along a direction to construct a rod shape, which broke the carbon nanostructure [Figure 6D]. In contrast, Se covered and

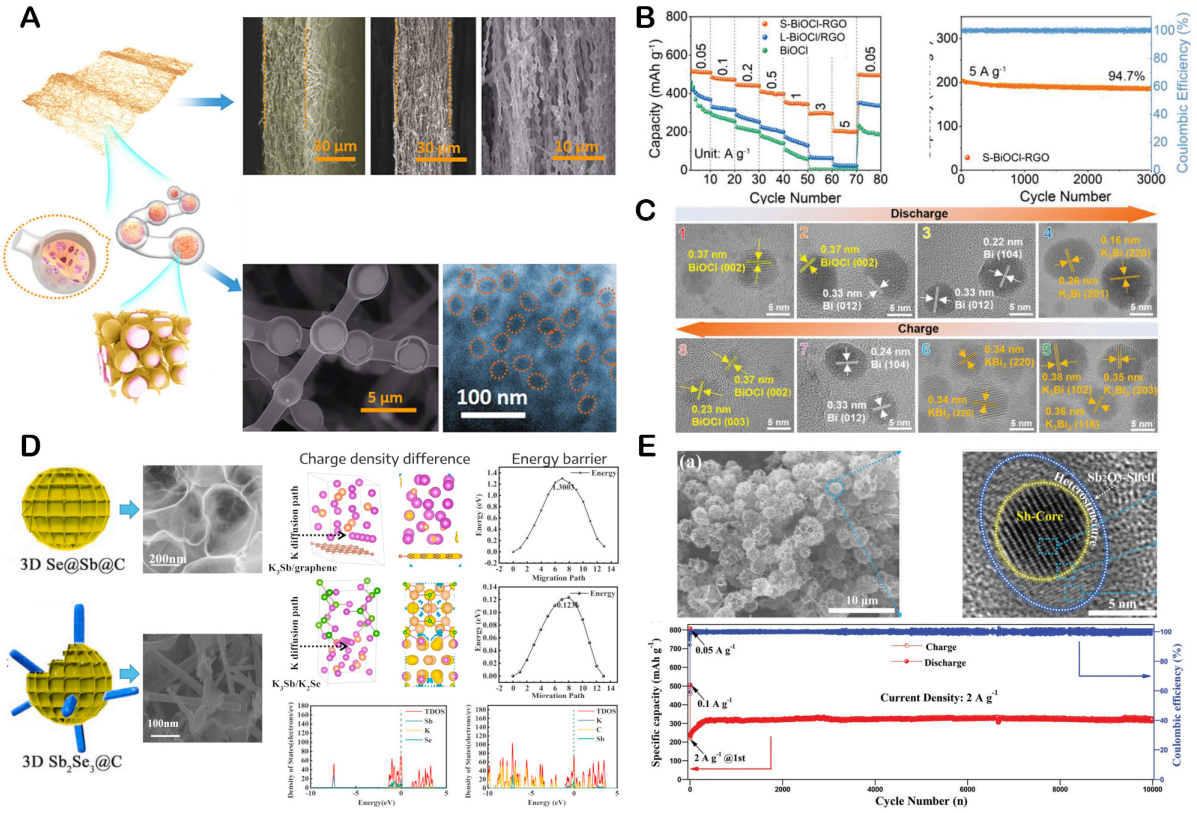

Figure 6. (A) Schematic illustration of the SnS_2@NSC flexible film and its morphology. Reprinted with permission from Ref.[78]. Copyright 2023, Elsevier. (B) Rate capability and cyclability of S-BiOCl-RGO, L-BiOCl/RGO, and BiOCl. (C) *Ex situ* HRTEM images for S-BiOCl-RGO anodes (1) discharge to 2.0 V, (2) discharge to 1.8 V, (3) discharge to 1.6 V, (4) discharge to 0.01 V, (5) charge to 0.8 V, (6) charge to 1.2 V, (7) charge to 1.6 V, and (8) charge to 2.0 V. Reprinted with permission from Ref.[79]. Copyright 2022, John Wiley and Sons. (D) Illustration and SEM images of 3D Se@Sb@C and 3D Sb_2Se_3@C and K diffusion paths in K_3Sb/graphene interface and K_3Sb/K_2Se interface and PDOS analysis between (Sb, K, and Se) and (Sb, K, and C). Reprinted with permission from Ref.[82]. Copyright 2020, Elsevier. (E) Morphology and cyclability of Sb@Sb_2O_3@N-3DCHs. Reprinted with permission from Ref.[83]. Copyright 2021, John Wiley and Sons.

chemically bonded with Sb to form Se@Sb particles with sizes of 10-22 nm in the original 3D carbon structure of 3D Sb. As a result, the 3D Se@Sb@C anode exhibited higher electrochemical performance than the Sb_2Se_3@C anode. It maintained a rate capability of 107.43 mAh g^{-1} at 10 A g^{-1} and long cyclability with a capacity of 166.6 mAh g^{-1} after 5,000 cycles at 5 A g^{-1}, corresponding to a capacity retention of 87%. To clarify the role of the heterostructure, the energy barrier for K^+ diffusion at the K_3Sb/C and K_3Sb/K_2Se interface was calculated using a DFT approach. K_3Sb/K_2Se was found to have a large number of charge interactions due to the formation of heterojunctions. Therefore, the diffusion energy of K^+ at K_3Sb/K_2Se was 0.1236 eV, which was approximately 10 times lower than that of K_3Sb/C (1.3003 eV) [Figure 6D]. In addition, according to the projected density of states results, the valence electrons of Sb, K, and Se were found to hybridize intensively, creating more electronic states that benefit K^+ migration, as mentioned earlier.

Subsequently, a core-shell heterostructure consisting of Sb@Sb_2O_3 embedded in 3D hollow N-doped carbon (Sb@Sb_2O_3@N-3DCHs) was synthesized by partially oxidizing Sb@N-3DCHs[83]. The thickness of the shell was carefully controlled to be within the range of 1-4 nm, as presented in Figure 6E. For comparison, a completely oxidized Sb_2O_3@N-3DCHs was also synthesized. Among them, the Sb@Sb_2O_3@N-3DCHs anode

exhibited excellent rate capability and highest specific capacities of 474, 433, 402, 373, 318, and 239 mAh g^{-1} at 0.1, 0.2, 0.5, 1, 2, and 5 A g^{-1}, respectively. Furthermore, for long-term cycling stability, the Sb@Sb_2O_3@N-3DCHs anode demonstrated an impressive capacity retention of 80.3% after 10,000 cycles at 2 A g^{-1}, delivering a capacity of 319 mAh g^{-1} with little capacity fading. This result confirms the advantage of core-shell heterostructures in improving the electrochemical performance of anode materials.

Phosphorus anode materials

In nature, phosphorus exists in three different allotropes: white, black, and red phosphorus. While white phosphorus is flammable and toxic, black phosphorus is a suitable anode material for PIBs due to its layered crystalline structure with a large interlayer of 5.2 Å and high electronic conductivity of 2-33 mS cm^{-1}[84]. However, pristine black phosphorus suffers from large volume changes during cycling, resulting in a low reversible capacity. To address this issue, Du *et al.* prepared a black phosphorus/graphite composite (BP/G) by mechanical ball milling and investigated the use of different electrolytes, including normal concentration electrolyte (NCE; 1 M KFSI in trimethyl phosphate (TMP)), high concentration electrolyte (HCE; 5M KFSI in TMP), and localized high concentration electrolyte (LHCE; KTFSI/TMP/1,1,2,2-tetrafluoroethyl-2,2,2-trifluoroethyl ether (HFE = 1/1.7/2%mol))[84]. LHCE was prepared by adding a dilute solvent (e.g., HFE) to locally increase the ion concentration without increasing the electrolyte viscosity, cost, or salt concentration. The synergistic effect of graphite coating and LHCE significantly improved the cyclability and rate capability of the BP/G anode. BP/G using LHCE delivered 618, 342, and 291 mAh g^{-1} at 0.1, 0.3, and 0.5 mA g^{-1}, respectively [Figure 7A]

Red phosphorus is also a promising candidate for anode due to its inexpensive and chemically stable properties. However, it also possesses poor conductivity and requires a composite of red phosphorus with high-conductivity buffer material. Red phosphorus was impregnated in N, S co-doped carbon nanofibers (RP@S-N-CNFs) as a free-standing anode material[85]. The use of HCE (5M KFSI in DME) electrolyte showed good cyclability with a capacity retention of 282 mAh g^{-1} after 2,000 cycles at 2 A g^{-1}.

Furthermore, high electrical conductivity metals, such as Bi or Sb, can be utilized as coating layers to address the poor conductivity of red phosphorus, as noted in previous studies[86]. Specifically, Bi nanoparticles were encapsulated in a 3D honeycomb-like porous red phosphorus (3D HPRP) structure to form HPRP@Bi. During the first few cycles, the Bi nanoparticles were transferred to the amorphous phase and covered the 3D HPRP structure, creating an electrical conducting network that improved the conductivity of HPRP@Bi [Figure 7B]. Moreover, the 3D HPRP structure helped to reduce the stress-strain caused by volume expansion during cycling. The diffusion energy barriers of HPRP@Bi (Amorphous), HPRP@Bi (Crystalline), and HPRP were calculated by DFT and found to be 0.3641, 0.4359, and 0.5117 eV, respectively. Therefore, HPRP@Bi (Amorphous) can promote fast K^+ diffusion, improving its rate capability. Compared with 3D HPRP, HPRP@Bi demonstrated an improved rate capability, delivering discharge capacities of 412.0, 383.7, 344.0, 320.4, 287.3, 231.6, 152.3, and 106.4 mA h g^{-1} at 0.05, 0.1, 0.2, 0.3, 0.5, 1, 2, and 3 A g^{-1}, respectively. HPRP@Bi also exhibited good long-term cyclability, delivering a specific capacity of 283 mAh g^{-1} after 200 cycles at 0.05 A g^{-1} with a capacity retention of 61%. The effectiveness of this concept was also successfully demonstrated using Sb as a coating layer. However, the cyclability of the resulting anode material is still not sufficient compared to using carbon coating, even with the use of HCE 4M KFSI. Another approach involves the use of metal phosphite as an anode material for PIBs. Previous studies have reported the successful utilization of various metal phosphides, such as tin phosphide[28] and zinc phosphide[87], as anode materials.

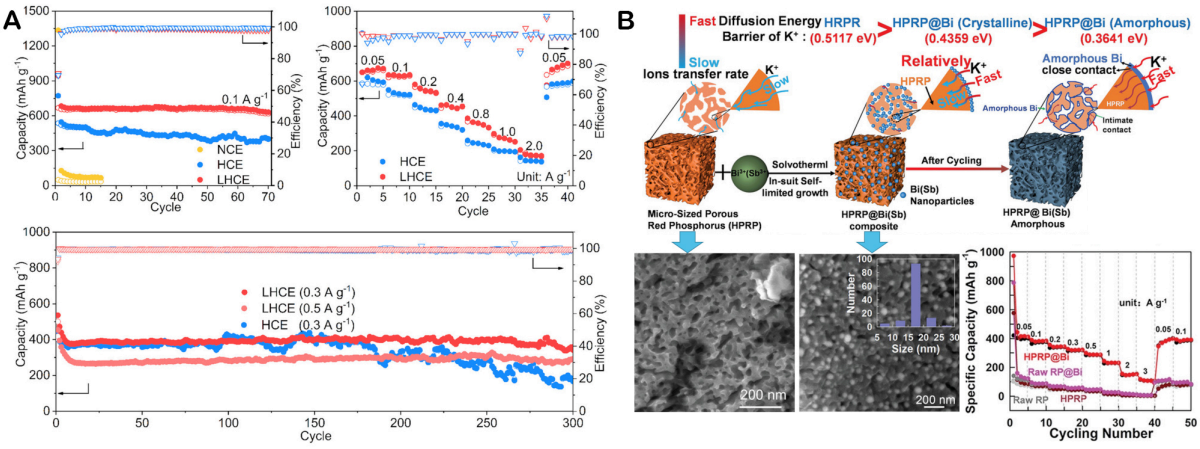

Figure 7. (A) Cyclability and rate capability of the BP/G composite using NCE, HCE, and LHCE. Reprinted with permission from Ref.[84]. Copyright 2021, American Chemical Society. (B) Schematic diagram of the fabrication of HPRP@Bi (HPRP@Sb) composite and its superior potassium storage mechanism. Reprinted with permission from Ref.[86]. Copyright 2022, John Wiley and Sons.

For a more comprehensive comparison, we summarized the electrochemical performance of typical alloy-based anode materials for PIBs in Table 3. Of these materials, Sb-based anodes are regarded as promising candidates due to their relatively high capacity. However, Bi-based anodes exhibit superior cyclability at high specific currents, making them well-suited for large-scale PIB applications.

Selenide compounds

Selenium-based anode materials (SnSe, Sb_2Se_3, and Bi_2Se_3) have garnered considerable interest due to their outstanding electrical conductivity and significant theoretical capacity for PIBs[25,80,90,91]. However, two primary challenges hinder the practical implementation of Se-based electrodes. Firstly, the pronounced volume variation during cycling induces agglomeration and cracking in Se-based electrodes, which substantially impairs performance[90]. Numerous efforts have been made to mitigate the volume change of Se-based electrodes, including the utilization of hybrid composites[65], morphological regulation[78], and nanocrystallization[23]. Nevertheless, the complex processes involved in these techniques may not be sufficiently efficient for practical production. Secondly, the shuttle effect of soluble intermediate polyselenides generated by the electrochemical reactions of Se-based electrodes leads to a continuous loss of active materials, ultimately causing irreversible capacity decay in batteries[64-66]. Based on current research, physical trapping and chemical bonding have been suggested as the most effective strategies to prevent the ongoing loss of active selenium species[90].

The aforementioned challenges can be addressed by employing multi-element combinations and carbon modification to enhance the electrochemical properties of selenides used as PIB anodes[68,80,92]. For instance, Yi *et al.* reported that layered SnSSe anodes provide high specific capacity and excellent cycling stability for PIBs, owing to the enlarged interlayer spacing, partial substitution of S by Se, and improvement of the electrical conductivity of the material with the assistance of multilayered graphene sheets[93]. Furthermore, Tian *et al.* developed a $SnSb_2Se_4$@GNS lamellar nanostructure, which comprises graphene nanosheets embedded with $SnSb_2Se_4$ nanoparticles[94]. This composite consists of finely dispersed $SnSb_2Se_4$ nanoparticles and graphene nanosheets, forming a porous network architecture. This structure is capable of effectively mitigating the significant volume changes that can occur during electrode reactions and ensuring efficient K-ion storage due to the synergistic interactions among various elements. Numerous electrochemical studies demonstrate that $SnSb_2Se_4$ inherits the advantages of the binary components (Sb_2Se_3 and SnSe) while

Table 3. Summary of the long-term performance of typical alloy-based anode materials for PIBs

Anode material	Electrolyte	Binder	Loading mass (mg cm^{-2})	Specific current (mA g^{-1})	Number of cycles	Specific capacity (mAh g^{-1})	Capacity retention	Ref.
Sb@MCMB-3	3M KFSI/DME	PVDF	1.0-1.2	1,000	500	300.1	89.80%	[26]
Sb SQ@MA	1M KFSI/EC-PC	CMC	1	1,000	1,000	314	94.00%	[29]
Sb@NSF-C	5M KFSI/DME	CMC	0.8-1.0	1,000	200	286.5	~82.3%	[30]
Sb@$Ni_3(HHTP)_2$	3M KFSI/EC-DMC	PAA	1.1	1,000	300	431	90.40%	[32]
Sb@PCNFs	0.8 KPF6/EC-DEC	No	0.6-0.8	500	2,000	314	~93.5%	[40]
Sb@NPC-2	4M KFSI/EC-DMC	PAA	1	800	500	360.8	75.70%	[47]
Bulk Sb	4M KFSI/DME	CMC + PAA	1.5	200	200	553	95.40%	[88]
Bi NSs/NCNs	1M KPF6/DME	CMC	0.6-1.0	10,000	2,000	457.8	~84.6%	[36]
2D-Bi	1M KPF6/DME	CMC	1	10,000	750	344	94.00%	[24]
2D Bi@NOC	1M KPF6/DME	PVDF	0.7-1.0	10,000	1,000	341.7	~85.3%	[45]
Bi@NC	1M KPF6/DME	CMC	0.8	5,000	2,000	299.3	80.00%	[49]
Bi@C	2M KFSI/EC-DEC	CMC	1.2	500	1,000	206	61.80%	[52]
Bi@N-CT	1M KPF6/DME	Na-PAA	-	3,850	1,000	266	88.00%	[56]
Bi@NS-C	1M KPF6/DME	PCDF	0.44	1,000	800	350.3	88.00%	[57]
Sn/N-CNFs-5	0.8 KPF6/EC-DEC	CMC	0.5-1.0	1,000	3,000	198	88.40%	[38]
SnSe@C	1M KTFSI/EC-DEC	PAA	1.1	500	1,000	203.4	100.00%	[25]
SnSb@MAC	4M KFSI/DME	CMC	0.8-0.9	500	5,000	200	71.60%	[59]
SnSb/C	1M KFSI/EC-DEC	CMC + PAA	-	1,000	800	~15.8	~4.5%	[89]
	3M KFSI/EC-DEC					~55.0	~16.4%	
	3M KFSI/DME					~270.0	72.2%	
SnTe/MGS	0.8M KPF6/EC-DEC	CMC	0.8	500	1,000	304.1	82.60%	[61]
Bi_2Te_3@C	0.5M KFSI/EC-DMC	CMC	3	1,000	500	204	79.80%	[27]
$Bi_{0.5}Sb_{0.5}$@P	4M KFSI/DME	CMC	0.8	500	800	294.5	~75.0%	[62]
BiSb@TCS	3M KFSI/EGDME	CMC-SBR	0.8	2,000	5,700	181	~100.0%	[63]
BiSb/CNT	4M KFSI/DME	CMC	0.4-0.8	500	6,000	184	~40.5%	[64]
BiSb@C	3M KFSI/DME	CMC	-	500	1,000	303.5	92.60%	[65]
Bi_2Se_3@NC	5M KFSI/DEGDME	CMC	1.0-1.5	500	2,000	167	~76.4%	[67]
$FeSb_2$@3DPC	4M KFSI/DME	Sodium alginate	0.4	500	4,000	242	98.80%	[70]
$BiSbO_4$ nanonetwork	1M KFSI/DMC	CMC + PAA	1.0-1.2	500	1,000	256.5	~87.7%	[73]
a-SnS@pCNFs-650	0.8M KPF6/EC-DEC	CMC	0.5-1.0	1,000	1,000	227.7	76.00%	[74]
YS-Sb_2S_3@NSC	5M KFSI/DME	CMC	1.0-1.1	1,000	2,000	248.4	~80.0%	[77]

SnS_2@NSC CSN	1M KPF6/EC-DEC	No	0.9	2,000	2,000	205.3	75.40%	[78]
S-BiOCl-RGO	1M KFSI/EC-DEC	No	4.21	5,000	3,000	194	94.70%	[79]
Sb/Sb_2S_3@CHT	4M KFSI/DME	CMC	0.5	1,000	3,500	147.5	44.80%	[31]
Bi_2S_3/Bi_2Se_3	1M KFSI/DMC	CMC	0.7-0.9	500	1,000	~140.0	~42.8%	[80]
3D Se@Sb@C	0.8M KFSI/EC-DEC	CMC	0.8	5,000	5,000	166.6	87.00%	[82]
$Sb@Sb_2O_3$@N-3DCHs	3M KFSI/DME	CMC	0.8-1.0	2,000	10,000	319	~100.0%	[83]
Black phosphorus/graphite	KFSI/TMP/HFE = 1:1.7:2 by mole	PAA	1	500	300	219	~100.0%	[84]
RP@S-N-CNFs	5M KFSI/DME	No	-	2,000	2,000	282	~141.0%	[85]

circumventing their limitations, thus illustrating the synergistic nature of the $SnSb_2Se_4$ system. The $SnSb_2Se_4$@GNS composite exhibits outstanding cycling behavior, retaining a specific capacity of 265.8 mAh g^{-1} after 500 cycles at a current density of 500 mA g^{-1}. These findings offer valuable insights into the design and fabrication of multi-element alloy-based ano

ELECTROLYTE AND BINDER

The electrolyte is a crucial component that directly affects the electrochemical performance of batteries. Various kinds of electrolytes have been studied, including non-aqueous, aqueous, ionic liquid, solid polymer, composite, and inorganic solid electrolytes[15]. Currently, non-aqueous electrolytes are widely used, while others are still in their infancy. However, research on electrolytes for PIBs may be accelerated by utilizing modern methods such as *in-situ*, operando, theoretical calculation, and artificial intelligence (AI), as well as drawing from their analogs (LIBs, SIBs). Non-aqueous electrolytes are typically composed of potassium salts (e.g., $KClO_4$, KPF_6, KFSI, KTFSI), organic solvents (e.g., esters such as ethylene carbonate (EC), propylene carbonate (PC), dimethyl carbonate (DMC), diethyl carbonate (DEC), and ethers such as dimethoxyethane (DME), diethylene glycoldimethyl ether (DEGDME), ethylene glycol diethyl ether (EGDE), *etc.*), and additives. Furthermore, Table 4 presents a summary of the crucial physicochemical characteristics of potassium salts and solvents used in PIB electrolytes. The organic solvent mostly affects the solvation/desolvation process of K^+ in the electrolyte, significantly influencing the performance of PIBs. Initially, a mixture of ester solvents (e.g., EC/DEC) was used to adjust both viscosity and dielectric constant. However, ester solvents may form incompatible SEI layers on the surface of the alloy anode[15]. Subsequently, ether solvents were investigated to stabilize the alloy anode. DME, in particular, has been extensively studied as a solvent for PIBs, as it forms a compatible solvation structure that significantly contributes to the high performance of alloy-based anodes. For example, a microsize Bi anode had a high capacity of 387 mAh g^{-1} and retained 94.4% of its capacity after 100 cycles at 500 mA g^{-1} when 1M KPF_6 in DME electrolyte was employed, which was significantly improved compared to 1M KPF_6 in PC[96]. Specifically, when using a carbonate solvent with low steric effect, PF_6^- has a higher probability of interacting with Na^+ in the solvation structure, leading to close proximity between PF_6^- and Na^+ and influencing the desolvation process. Moreover, other anions, such as $CF_3SO_3^-$ and ClO_4^-, can also occupy the position of DME in the solvation structure, leading to an unstable alloying process. Du *et al.* stabilized the microsize Sb by constructing a 1 M KFSI-EGDE electrolyte-derived elastic SEI layer to confine the Sb during cycling[97].

Table 4. Physicochemical characteristics of potassium salts and solvents reported for PIB electrolytes[95]

Salt	Cost	Molar mass ($g\ mol^{-1}$)	Decomposition temperature (°C)	Solubility ($mol\ kg^{-1}$)	Conductivity ($mS\ cm^{-1}$)	Toxicity
KPF_6	Low cost	184.06	575	PC: 0.9 DME: 1.8	5.75	Low toxicity
KFSI	High cost	219.23	102	Hardly dissolved in PC	7.2	Nontoxic
KTFSI	High cost	319.24	198-203	Hardly dissolved in PC	6.1	Nontoxic
$KClO_4$	Low cost	138.55	610	PC: 10 DME: 7.5	1.1	Highly toxic
KBF_4	Highly cost	125.90	530	DME: 6	0.2	Highly toxic
KCF_3SO_3	High cost	188.17	238.5	Water: 22	-	Nontoxic
Solvent	**Melting point (°C)**	**Boiling point (°C)**	**Flash point (°C)**	**Density 25 °C ($g\ mL^{-1}$)**	**Viscosity at 25 °C (cP)**	**Dielectric constant at 25 °C**
PC	-48.8	242	132	1.20	2.5	0.0 ± 0.4
EC	36.4	248	160	1.32	2.1	0.0 ± 0.5
DMC	0.5	91	18	1.07	0.6	56 ± 0.1
DEC	-43	126	31	0.98	0.8	11.5 ± 0.2
DEGDME	-64	162	57	0.94	1.1	3.2 ± 0.2
DME	-69	84	0	0.87	0.5	80.6 ± 0.1

Subsequently, an HCE (4M KFSI in DME) was subsequently reported for the microsize Sb anode[88]. The high performance of the Sb anode is primarily attributed to the tuning of the K^+ solvation structure by controlling the electrolyte composition. In a compatible electrolyte (e.g., 4M KFSI in DME), K^+ de-solvates to form K^+-solvent-anion complexes. This complex accepts electrons and releases K^+ to alloy with Sb [Figure 8A]. In contrast, in an incompatible electrolyte (e.g., 1 M KFSI in EC/EMC), electrons tend to transfer from K^+ to the solvent, decomposing the electrolyte to form the SEI layer [Figure 8B] The structure of the K^+-solvent-anion complex, rather than the SEI layer, is the primary determinant of the performance of Sb and the anode for PIBs. However, high-concentration electrolytes may reduce the energy density when it is counted for the total mass of PIBs. Moreover, the high-concentration electrolyte may exceed the optimized concentration to reach the highest ionic conductivity value. For this reason, localized high-concentration electrolytes, new low-concentration electrolytes, and weakly solvating electrolytes for alloy anodes need to be further investigated[98-100].

The binder is an important component of the electrode and has a direct impact on electrode performance. (PAA, carboxymethyl cellulose (CMC), and their derivatives were favorable to prolonging the stability of the alloy anode by forming hydrogen bonding between the hydroxyl of the binder with anode particles[24,25,47,82,94-96]. For example, the chemically interlinked carboxymethyl cellulose with polyacrylic acid (CMC + PAA) binder has been shown to boost the cyclability and rate capability of the microsize SnSb/C anode[94]. The improvement is attributed to the high viscoelastic properties of CMC + PAA, which

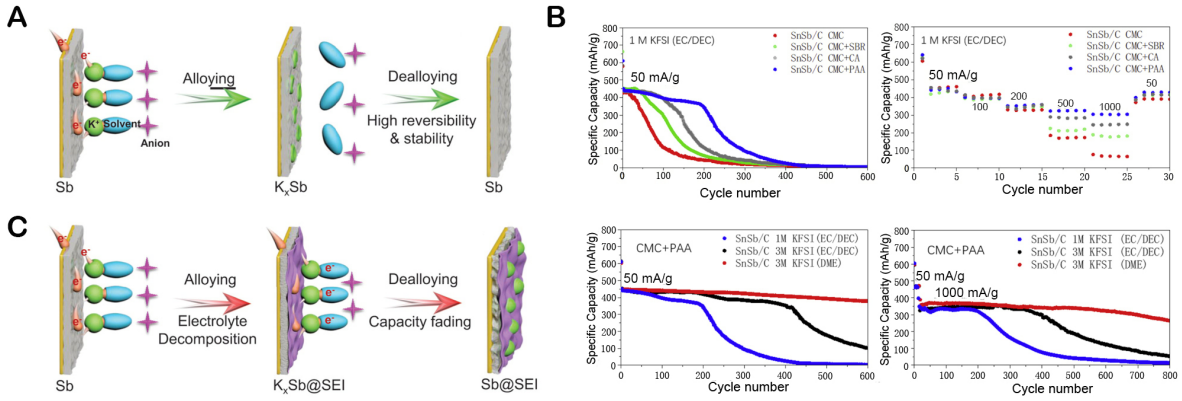

Figure 8. Comparative reaction pathways for K^+-solvent structure: (A) a reversible K^+ (de-) alloying process. (B) an electrolyte (i.e. K^+-solvent-anion) decomposition process that can be observed on the Sb electrode surface. Reprinted with permission from Ref.[88]. Copyright 2021, John Wiley and Sons. (C) Cycling performance of SnSb/C with various binders and electrolytes. Reprinted with permission from Ref.[89]. Copyright 2020, Elsevier.

inhibit the stress during volume expansion of the anode. CMC + PAA further cooperated with 3M KFSI in DME. As shown in Figure 8C, the SnSb/C electrode could maintain capacities of 419 mAh g^{-1} at 50 mA g^{-1} and 340 mAh g^{-1} at 1,000 mA g^{-1} over 600 and 800 cycles, respectively. Therefore, there is still a demand to develop high-elastic and self-healing binders for PIBs, which will require further effort.

Additionally, Table 3 also provides the electrochemical performance of typical alloy-based anode materials for PIBs, including information on electrolytes and binders. Based on the data presented, high-concentration or ether-based electrolytes and CMC or PAA binders appear to receive more attention for utilizing alloy anodes.

CONCLUSION AND OUTLOOK

This review provides a comprehensive summary of recent progress in developing alloy anode materials for PIBs. The developed alloy anode materials for PIBs have been thoroughly evaluated and discussed in terms of their strengths and weaknesses. Alloy anode materials with high theoretical capacities and low potassiation potentials are considered promising for PIBs. However, their large volume changes during the potassiation/depotassiation process result in poor cycling performance, hindering their practical use. To overcome these limitations, researchers have focused on strategies such as nanostructure and heterostructure design, engineering alloys, and combining them with conductive matrixes. These approaches have been successful in reducing volume changes, improving conductivity, and enhancing the kinetics of redox reactions, thereby boosting cyclability and rate performance. Additionally, the morphology of anodes can be more easily controlled through bottom-up or top-down approaches, which is beneficial for electrode fabrication. Moreover, the oxide, sulfide, and oxyhalide compounds of alloy metal-metalloids have also been reviewed as potential anode materials due to their lower cost and high theoretical capacities.

In spite of the recent progress and enhancements in the performance of alloy anode materials, further research is necessary to improve their capacity and stability to fulfill the practical demands of PIBs. In general, there are several challenges that still need to be tackled, ranging from fundamental to practical applications, including:

1. Despite significant research efforts, the commercialization of PIBs remains challenging due to the current laboratory-scale nanostructure design of alloy anodes. To address this limitation, research is ongoing to develop simplified and cost-effective methods for preparing alloying anodes, and the integration of AI is being explored to accelerate anode development. By combining these methods, compute-assisted material design, optimized preparation, composition control, and interface manipulation can be accomplished, leading to outstanding anode properties.

2. Both theoretical and experimental approaches are critical for revealing the comprehensive reaction mechanisms of alloy anodes. Density functional theory and molecular dynamics simulations can provide theoretical approaches to explain the mechanism of electrochemical reactions, SEI formation, and ion migration inside batteries. In addition, *in-situ* and operando characterization can directly observe the phase transition and volume expansion of active materials during charge and discharge and further shed light on the potassiation/depotasiation mechanism of PIBs.

3. While the reaction mechanism of the anode has been extensively studied, the failure mechanisms of alloy-based electrodes are not well understood. A deeper understanding of the failure mechanisms of alloy-based electrodes is essential for designing anode structures. In half-cells, the degradation of batteries may originate from the metallic potassium side, so the impact of metallic potassium on the degradation of half-cells should be considered. To avoid this problem, the investigation of full-cells is helpful in evaluating electrochemical performance. Additionally, the early prediction of the lifetime for anode materials and full-cell PIBs should be investigated with AI assistance.

4. Designing nanostructures to reduce the large volume expansion of alloy-based anodes will lessen the tap density of the anode and the volumetric capacity of batteries. The degradation caused by the volume expansion becomes more severe at high loading mass, resulting in rapid capacity fading. Future research should focus on the electrochemical performance at high loading mass. In this aspect, the composite of alloy anode materials with carbon and other conductive materials could provide a balance between cycling stability and capacity that is suitable for commercialization.

5. Optimizing the electrolyte is also a key factor in upgrading the performance of the battery. A compatible electrolyte should exhibit sufficient ionic conductivity at the evaluated temperature and proper solvation structure and promote the formation of a thin and elastic SEI. More research is needed to explore more stable and safer electrolytes for high-performance alloy-based anodes and understand the underlying mechanisms using both theoretical and experimental approaches.

6. The binder used in the battery also plays a crucial role in its performance. Optimizing the binder is expected to improve the anode performance of PIBs. However, research on binders is still in the early stages, and more attention needs to be given to this aspect.

7. The synthesis of most alloy anodes is currently limited to laboratory-scale production, as there is no synthetic procedure that meets the requirements for large-scale industrial production. Hence, the development of a large-scale and efficient synthesis method is necessary.

The design strategies and perspectives for enhancing alloy-based anodes presented in this review can also be applied to improve the performance of other types of electrode materials for rechargeable batteries. It is expected that this review will serve as an inspiration for researchers and contribute to the advancement of anode materials not only for PIBs but also for other battery technologies.

DECLARATIONS

Acknowledgments

The author Dr. Rakesh would like to thank Central University of Allahabad for providing a research facility.

Authors' contributions

Proposed the topic of this review: Verma R
Prepared the manuscript: Nguyen AG, Verma R, Didwal PN
Collectively discussed and revised the manuscript: Nguyen AG, Verma R, Didwal PN, Park CJ
Writing - review and editing, Conceptualization, and supervision: Verma R, Park CJ

Availability of data and materials

Not applicable.

Financial support and sponsorship

None.

Conflicts of interest

All authors declared that there are no conflicts of interest.

Ethical approval and consent to participate

Not applicable.

Consent for publication

Not applicable.

REFERENCES

1. Chang H, Wu Y, Han X, Yi T. Recent developments in advanced anode materials for lithium-ion batteries. *Energy Mater* 2021;1:100003. DOI
2. Bashir T, Ismail SA, Song Y, et al. A review of the energy storage aspects of chemical elements for lithium-ion based batteries. *Energy Mater* 2021;1:100019. DOI
3. Yan Y, Zeng T, Liu S, Shu C, Zeng Y. Lithium metal stabilization for next-generation lithium-based batteries: from fundamental chemistry to advanced characterization and effective protection. *Energy Mater* 2023;3:300002. DOI
4. Nazir A, Le HT, Nguyen A, Park C. Graphene analogue metal organic framework with superior capacity and rate capability as an anode for lithium ion batteries. *Electrochim Acta* 2021;389:138750. DOI
5. Nguyen A, Park C. Insights into tailoring composite solid polymer electrolytes for solid-state lithium batteries. *J Membr Sci* 2023;675:121552. DOI
6. Vu D, Kim D, Nguyen A, Park C. Stabilizing interface of novel 3D-hierarchical porous carbon for high-performance lithium-sulfur batteries. *Electrochim Acta* 2022;418:140369. DOI
7. Kim H, Ngo DT, Verma R, et al. Vanadium nitride and carbon nanofiber composite membrane as an interlayer for extended life cycle lithium-sulphur batteries. *Ceram Int* 2021;47:21476-89. DOI
8. Nguyen A, Le HT, Verma R, Vu D, Park C. Boosting sodium-ion battery performance using an antimony nanoparticle self-embedded in a 3D nitrogen-doped carbon framework anode. *Chem Eng J* 2022;429:132359. DOI
9. Verma R, Singhbabu YN, Didwal PN, Nguyen A, Kim J, Park C. Biowaste orange peel-derived mesoporous carbon as a cost-effective anode material with ultra-stable cyclability for potassium-ion batteries. *Batteries Supercaps* 2020;3:1099-111. DOI
10. Didwal PN, Verma R, Nguyen AG, Ramasamy HV, Lee GH, Park CJ. Improving cyclability of all-solid-state batteries via stabilized electrolyte-electrode interface with additive in poly (propylene carbonate) based Solid Electrolyte. *Adv Sci* 2022;9:2105448. DOI PubMed PMC
11. Sung B, Didwal PN, Verma R, Nguyen A, Chang DR, Park C. Composite solid electrolyte comprising poly (propylene carbonate) and $Li_{1.5}Al_{0.5}Ge_{1.5}(PO_4)_3$ for long-life all-solid-state Li-ion batteries. *Electrochim Acta* 2021;392:139007. DOI
12. Woo M, Didwal PN, Kim H, et al. Reinforcing effect of single-wall carbon nanotubes on the $LiNi_{0.6}Co_{0.2}Mn_{0.2}O_2$ composite cathode

for high-energy-density all-solid-state Li-ion batteries. *Appl Surf Sci* 2021;568:150934. DOI

13. Li G, Guo S, Xiang B, et al. Recent advances and perspectives of microsized alloying-type porous anode materials in high-performance Li- and Na-ion batteries. *Energy Mater* 2022;2:200020. DOI
14. Haynes WM. CRC handbook of chemistry and physics. 97th ed. Boca Raton: CRC Press; 2016. p. 2670. DOI
15. Verma R, Didwal PN, Hwang J, Park C. Recent progress in electrolyte development and design strategies for next-generation potassium-ion batteries. *Batteries Supercaps* 2021;4:1428-50. DOI
16. Zhang J, Lai L, Wang H, Chen M, Shen ZX. Energy storage mechanisms of anode materials for potassium ion batteries. *Mater Today Energy* 2021;21:100747. DOI
17. Liu J, Yin T, Tian B, et al. Unraveling the potassium storage mechanism in graphite foam. *Adv Energy Mater* 2019;9:1900579. DOI
18. Yuan F, Zhang D, Li Z, et al. Unraveling the intercorrelation between micro/mesopores and K migration behavior in hard carbon. *Small* 2022;18:2107113. DOI
19. Song K, Liu C, Mi L, Chou S, Chen W, Shen C. Recent progress on the alloy-based anode for sodium-ion batteries and potassium-ion batteries. *Small* 2021;17:1903194. DOI PubMed
20. Kim H, Kim JC, Bianchini M, Seo D, Rodriguez-garcia J, Ceder G. Recent progress and perspective in electrode materials for K-ion batteries. *Adv Energy Mater* 2018;8:1702384. DOI
21. Qi S, Deng J, Zhang W, Feng Y, Ma J. Recent advances in alloy-based anode materials for potassium ion batteries. *Rare Metals* 2020;39:970-88. DOI
22. Wang Q, Zhao X, Ni C, et al. Reaction and capacity-fading mechanisms of tin nanoparticles in potassium-ion batteries. *J Phys Chem C* 2017;121:12652-7. DOI
23. Liu X, Zhu J, Yue L, et al. Green and scalable template-free strategy to fabricate honeycomb-like interconnected porous micro-sized layered sb for high-performance potassium storage. *Small* 2022;18:2204552. DOI
24. Cheng X, Sun Y, Li D, et al. From 0D to 3D: dimensional control of bismuth for potassium storage with superb kinetics and cycling stability. *Adv Energy Mater* 2021;11:2102263. DOI
25. Verma R, Didwal PN, Nguyen A, Park C. SnSe nanocomposite chemically-bonded with carbon-coating as an anode material for K-ion batteries with outstanding capacity and cyclability. *Chem Eng J* 2021;421:129988. DOI
26. Ji F, Liu T, Li Y, Li D, Ci L. Ball-milling strategy for fast and stable potassium-ion storage in antimony-carbon composite anodes. *Chemelectrochem* 2020;7:4587-93. DOI
27. Ko JK, Jo JH, Kim HJ, et al. Bismuth telluride anode boosting highly reversible electrochemical activity for potassium storage. *Energy Stor Mater* 2021;43:411-21. DOI
28. Verma R, Didwal PN, Ki HS, Cao G, Park CJ. SnP_3/carbon nanocomposite as an anode material for potassium-ion batteries. *ACS Appl Mater Inter* 2019;11:26976-84. DOI
29. Guo X, Gao H, Wang S, et al. MXene-based aerogel anchored with antimony single atoms and quantum dots for high-performance potassium-ion batteries. *Nano Lett* 2022;22:1225-32. DOI
30. Shi X, Liu W, Zhao S, et al. Integrated anodes from heteroatoms (N, S, and F) co-doping antimony/carbon composite for efficient alkaline ion (Li^+/K^+) storage. *ACS Appl Energy Mater* 2022;5:12925-36. DOI
31. Wu Y, Zheng J, Tong Y, et al. Carbon hollow tube-confined Sb/Sb_2S_3 nanorod fragments as highly stable anodes for potassium-ion batteries. *ACS Appl Mater Inter* 2021;13:51066-77. DOI
32. Nazir A, Le HT, Nguyen A, Kim J, Park C. Conductive metal organic framework mediated Sb nanoparticles as high-capacity anodes for rechargeable potassium-ion batteries. *Chem Eng J* 2022;450:138408. DOI
33. Verma R, R K, Varadaraju U. In-situ carbon coated $CuCo_2S_4$ anode material for Li-ion battery applications. *Appl Surf Sci* 2017;418:30-39. DOI
34. Xue J, Wu T, Dai Y, Xia Y. Electrospinning and electrospun nanofibers: methods, materials, and applications. *Chem Rev* 2019;119:5298-415. DOI PubMed PMC
35. Tian Z, Chui N, Lian R, et al. Dual anionic vacancies on carbon nanofiber threaded MoSSe arrays: a free-standing anode for high-performance potassium-ion storage. *Energy Stor Mater* 2020;27:591-8. DOI
36. Cui RC, Zhou HY, Li JC, Yang CC, Jiang Q. Ball-cactus-like Bi embedded in N-riched carbon nanonetworks enables the best potassium storage performance. *Adv Funct Mater* 2021;31:2103067. DOI
37. Cao K, Liu H, Jia Y, et al. Flexible antimony@carbon integrated anode for high-performance potassium-ion battery. *Adv Mater Technol* 2020;5:2000199. DOI
38. Li C, Bi AT, Chen HL, et al. Rational design of porous Sn nanospheres/N-doped carbon nanofibers as an ultra-stable potassium-ion battery anode material. *J Mater Chem A* 2021;9:5740-50. DOI
39. Lin X, Xue F, Zhang Z, Li Q. Sb nanoparticles encapsulated in N-doped carbon nanotubes as freestanding anodes for high-performance lithium and potassium ion batteries. *Rare Metals* 2023;42:449-58. DOI
40. Chen Q, Li H, Li H, et al. Freestanding film formed with Sb-nanoplates embedded in flexible porous carbon nanofibers as a binder-free anode for high-performance wearable potassium-ion battery. *Chin Chem Lett* 2023;34:107402. DOI
41. He X, Liao J, Wang S, et al. From nanomelting to nanobeads: nanostructured Sb_xBi_{1-x} alloys anchored in three-dimensional carbon frameworks as a high-performance anode for potassium-ion batteries. *J Mater Chem A* 2019;7:27041-7. DOI
42. Xiong P, Wu J, Zhou M, Xu Y. Bismuth-antimony alloy nanoparticle@porous carbon nanosheet composite anode for high-performance potassium-ion batteries. *ACS Nano* 2020;14:1018-26. DOI

43. Imtiaz S, Kapuria N, Amiinu IS, et al. Directly deposited antimony on a copper silicide nanowire array as a high-performance potassium-ion battery anode with a long cycle life. *Adv Funct Mater* 2023;33:2209566. DOI
44. Yang Y, Shi W, Leng S, Cheng H. Multidimensional antimony nanomaterials tailored by electrochemical engineering for advanced sodium-ion and potassium-ion batteries. *J. Colloid Interf Sci* 2022;628:41-52. DOI
45. Xu A, Zhu Q, Li G, et al. 2D bismuth@N-doped carbon sheets for ultrahigh rate and stable potassium storage. *Small* 2022;18:2203976. DOI
46. An Y, Tian Y, Ci L, Xiong S, Feng J, Qian Y. Micron-sized nanoporous antimony with tunable porosity for high-performance potassium-ion batteries. *ACS Nano* 2018;12:12932-40. DOI
47. Verma R, Nguyen A, Didwal PN, Moon C, Kim J, Park C. In-situ synthesis of antimony nanoparticles encapsulated in nitrogen-doped porous carbon framework as high performance anode material for potassium-ion batteries. *Chem Eng J* 2022;446:137302. DOI
48. Chen N, Shen N, Yi X, et al. Achieving stable K-storage performance of carbon sphere-confined Sb via electrolyte regulation. *J Energy Chem* 2023;76:51-8. DOI
49. Liu X, Sun Y, Tong Y, Li H. Unique Spindle-like bismuth-based composite toward ultrafast potassium storage. *Small* 2022;18:2204045. DOI
50. Ababaikeri R, Sun Y, Wang X, et al. Scalable fabrication of Bi@N-doped carbon as anodes for sodium/potassium-ion batteries with enhanced electrochemical performances. *J Alloys Compd* 2023;935:168207. DOI
51. Liu X, Yu X, Tong Y, et al. Potassium storage in bismuth nanoparticles embedded in N-doped porous carbon facilitated by ether-based electrolyte. *Chem Eng J* 2022;446:137329. DOI
52. Yao J, Zhang C, Yang G, et al. Bismuth nanoparticles confined in carbonaceous nanospheres as anodes for high-performance potassium-ion batteries. *ACS Appl Mater Inter* 2021;13:31766-74. DOI
53. Zhang P, Zhu Q, Wei Y, Xu B. Achieving stable and fast potassium storage of Sb_2S_3@MXene anode via interfacial bonding and electrolyte chemistry. *Chem Eng J* 2023;451:138891. DOI
54. Shi Y, Zhou D, Wu T, Xiao Z. Deciphering the $Sb_4O_5Cl_2$-MXene hybrid as a potential anode material for advanced potassium-ion batteries. *ACS Appl Mater Inter* 2022;14:29905-15. DOI
55. Xiang X, Liu D, Zhu X, et al. Evaporation-induced formation of hollow bismuth@N-doped carbon nanorods for enhanced electrochemical potassium storage. *Appl Surf Sci* 2020;514:145947. DOI
56. Li H, Zhao C, Yin Y, et al. N-Doped carbon coated bismuth nanorods with a hollow structure as an anode for superior-performance potassium-ion batteries. *Nanoscale* 2020;12:4309-13. DOI
57. Long H, Yin X, Wang X, Zhao Y, Yan L. Bismuth nanorods confined in hollow carbon structures for high performance sodium- and potassium-ion batteries. *J Energy Chem* 2022;67:787-96. DOI
58. Ouyang D, Wang C, Zhu H, Yu F, Yin J. Bismuth nanoparticles encapsulated in mesoporous carbon nanofibers for efficient potassium-ion storage. *ACS Appl Nano Mater* 2022;5:13171-9. DOI
59. Hsieh Y, Chen K, Tuan H. A synergetic SnSb-amorphous carbon composites prepared from polyesterification process as an ultrastable potassium-ion battery anode. *Chem Eng J* 2021;420:130451. DOI
60. Shi X, Liu W, Zhang D, et al. Nanoscale localized growth of SnSb for general-purpose high performance alkali (Li, Na, K) ion storage. *Chem Eng J* 2022;431:134318. DOI
61. Du Y, Yi Z, Zhang Z, et al. A highly stable potassium-ion battery anode enabled by multilayer graphene sheets embedded with SnTe nanoparticles. *Chem Eng J* 2022;435:135100. DOI
62. Chen KT, Tuan HY. Bi-Sb nanocrystals embedded in phosphorus as high-performance potassium ion battery electrodes. *ACS Nano* 2020;14:11648-61. DOI PubMed
63. Huang C, Xu A, Li G, et al. Alloyed BiSb nanoparticles confined in tremella-like carbon microspheres for ultralong-life potassium ion batteries. *Small* 2021;17:2100685. DOI
64. Chen K, Yang Y, Lyu L, Lu M, Tuan H. In situ formed robust submicron-sized nanocrystalline aggregates enable highly-reversible potassium ion storage. *Nano Energy* 2021;88:106233. DOI
65. Wu Q, Chen B, Xie H, et al. Bismuth-antimony alloy nanoparticles encapsulated in 3D carbon framework: synergistic effect for enhancing interfacial potassium storage. *Chem Eng J* 2022;430:132906. DOI
66. Luo Q, Wen J, Liu G, et al. Sb_2Se_3/Sb embedded in carbon nanofibers as flexible and twistable anode for potassium-ion batteries. *J Power Sources* 2022;545:231917. DOI
67. Sun X, Zhang B, Chen M, et al. Space-confined growth of Bi_2Se_3 nanosheets encapsulated in N-doped carbon shell lollipop-like composite for full/half potassium-ion and lithium-ion batteries. *Nano Today* 2022;43:101408. DOI
68. Lin W, Yang Y, Tuan H. Ternary chalcogenide anodes for high-performance potassium-ion batteries and hybrid capacitors via composition-mediated bond softening and intermediate phase. *Energy Stor Mater* 2022;51:38-53. DOI
69. Zhang Y, Li M, Huang F, et al. 3D porous Sb-Co nanocomposites as advanced anodes for sodium-ion batteries and potassium-ion batteries. *Appl Surf Sci* 2020;499:143907. DOI
70. Wu Y, Sun Y, Tong Y, Li H. $FeSb_2$ nanoparticles embedded in 3D porous carbon framework: an robust anode material for potassium storage with long activation process. *Small* 2022;18:2201934. DOI
71. Su M, Li J, He K, et al. NiSb/nitrogen-doped carbon derived from Ni-based framework as advanced anode for lithium-ion batteries. *J Colloid Interf Sci* 2023;629:83-91. DOI

72. Qian M, Zhang W, Luo G, Wu C, Qin W. Air-stabilized pore structure engineering of antimony-based anode by electrospinning for potassium ion batteries. *J Colloid Interf Sci* 2023;633:352-61. DOI
73. Chang CH, Chen KT, Hsieh YY, Chang CB, Tuan HY. Crystal facet and architecture engineering of metal oxide nanonetwork anodes for high-performance potassium ion batteries and hybrid capacitors. *ACS Nano* 2022;16:1486-501. DOI PubMed
74. Li R, Wu J, He J, et al. Embedding amorphous SnS in electrospun porous carbon nanofibers for efficient potassium storage with ultralong cycle life. *Compos B Eng* 2022;243:110132. DOI
75. He Y, Xu Y, Zhang M, et al. Confining ultrafine SnS nanoparticles in hollow multichannel carbon nanofibers for boosting potassium storage properties. *Sci Bull* 2022;67:151-60. DOI
76. Yuan L, Zhou Q, Li T, Wang Y, Liu Z, Chong S. Promoting superior K-ion storage of Bi_2S_3 nanorod anode via graphene physicochemical protection and electrolyte stabilization effect. *Appl Energ* 2022;322:119471. DOI
77. Xiao B, Zhang H, Sun Z, et al. Achieving high-capacity and long-life K^+ storage enabled by constructing yolk-shell Sb_2S_3@N, S-doped carbon nanorod anodes. *J Energy Chem* 2023;76:547-56. DOI
78. Si J, Liu X, Wang Z, Zhang S, Deng C. Confining SnS_2@N, S codoped carbon in core-shell beads of necklace-like fibers towards ultrastable anode for flexible potassium-ion battery. *J Energy Chem* 2023;76:349-58. DOI
79. Hao G, Zhang C, Chen Z, Xu Y. Nanoconfinement synthesis of ultrasmall bismuth oxyhalide nanocrystals with size-induced fully reversible potassium-ion storage and ultrahigh volumetric capacity. *Adv Funct Mater* 2022;32:2201352. DOI
80. Hsieh Y, Tuan H. Architectural van der Waals Bi_2S_3/Bi_2Se_3 topological heterostructure as a superior potassium-ion storage material. *Energy Stor Mater* 2022;51:789-805. DOI
81. Suo G, Zhang J, Li R, Ma Z, Cheng Y, Ahmed SM. Antimony anchored in MoS_2 nanosheets with N-doped carbon coating to boost potassium storage performance. *Mater Today Chem* 2023;27:101300. DOI
82. Zhao N, Qin J, Chu L, et al. Heterogeneous interface of Se@Sb@C boosting potassium storage. *Nano Energy* 2020;78:105345. DOI
83. Chen B, Yang L, Bai X, et al. Heterostructure engineering of core-shelled Sb@Sb_2O_3 encapsulated in 3D N-doped carbon hollow-spheres for superior sodium/potassium storage. *Small* 2021;17:2006824. DOI
84. Du X, Zhang B. Robust solid electrolyte interphases in localized high concentration electrolytes boosting black phosphorus anode for potassium-ion batteries. *ACS Nano* 2021;15:16851-60. DOI PubMed
85. Feng W, Wang H, Jiang Y, et al. A strain-relaxation red phosphorus freestanding anode for non-aqueous potassium ion batteries. *Adv Energy Mater* 2022;12:2103343. DOI
86. Liu X, Zhu J, Wang X, et al. Boosting potassium storage kinetics, stability, and volumetric performance of honeycomb-like porous red phosphorus via in situ embedding self-growing conductive nano-metal networks. *Adv Funct Mater* 2023;33:2209388. DOI
87. Ji S, Song C, Li J, et al. Metal phosphides embedded with in situ-formed metal phosphate impurities as buffer materials for high-performance potassium-ion batteries. *Adv Energy Mater* 2021;11:2101413. DOI
88. Zhou L, Cao Z, Zhang J, et al. Electrolyte-mediated stabilization of high-capacity micro-sized antimony anodes for potassium-ion batteries. *Adv Mater* 2021;33:2005993. DOI
89. Wu J, Zhang Q, Liu S, et al. Synergy of binders and electrolytes in enabling microsized alloy anodes for high performance potassium-ion batteries. *Nano Energy* 2020;77:105118. DOI
90. Yang Z, Li W, Zhang G, et al. Constructing Sb-O-C bond to improve the alloying reaction reversibility of free-standing Sb_2Se_3 nanorods for potassium-ion batteries. *Nano Energy* 2022;93:106764. DOI
91. Li W, Yang Z, Zuo J, Wang J, Li X. Emerging carbon-based flexible anodes for potassium-ion batteries: progress and opportunities. *Front Chem* 2022;10:1002540. DOI PubMed PMC
92. Wang B, Zhang Z, Yuan F, et al. An insight into the initial coulombic efficiency of carbon-based anode materials for potassium-ion batteries. *Chem Eng J* 2022;428:131093. DOI
93. Yi Z, Xu J, Xu Z, et al. Ultrafine SnSSe/multilayer graphene nanosheet nanocomposite as a high-performance anode material for potassium-ion half/full batteries. *J Energy Chem* 2021;60:241-8. DOI
94. Tian R, Duan L, Xu Y, et al. Coupling ternary selenide $SnSb_2Se_4$ with graphene nanosheets for high-performance potassium-ion batteries. *Energy Environ Mater* 2023:e12617. DOI
95. Yuan F, Li Z, Zhang D, et al. Fundamental understanding and research progress on the interfacial behaviors for potassium-ion battery anode. *Adv Sci* 2022;9:2200683. DOI PubMed PMC
96. Zhou L, Cao Z, Wahyudi W, et al. Electrolyte engineering enables high stability and capacity alloying anodes for sodium and potassium ion batteries. *ACS Energy Lett* 2020;5:766-76. DOI
97. Du X, Gao Y, Zhang B. Building elastic solid electrolyte interphases for stabilizing microsized antimony anodes in potassium ion batteries. *Adv Funct Mater* 2021;31:2102562. DOI
98. Lv L, Zhang H, Lu D, et al. A low-concentration sulfone electrolyte enables high-voltage chemistry of lithium-ion batteries. *Energy Mater* 2022;2:200030. DOI
99. Xiao Y, Xu R, Xu L, Ding J, Huang J. Recent advances in anion-derived SEIs for fast-charging and stable lithium batteries. *Energy Mater* 2021;1:100013. DOI
100. Xiao W, Shi P, Li Z, et al. Regulating solid electrolyte interphases on phosphorus/carbon anodes via localized high-concentration electrolytes for potassium-ion batteries. *J Energy Chem* 2023;78:589-605. DOI